A SEISMIC REFLECTION STUDY
OVER THE BANE ANTICLINE
IN GILES COUNTY, VIRGINIA

by

Robert W. Edsall, Jr.

Thesis submitted to the Graduate Faculty of the
Virginia Polytechnic Institute and State University
in partial fulfillment of the requirements for the degree of
MASTER OF SCIENCE

in

Geophysics

APPROVED:

J. K. Costain, Chairman

E. S. Robinson

W. D. Lowry

G. A. Bollinger

G. C. Grender

February, 1974

Blacksburg, Virginia

INTRODUCTION

Appalachian geology, because of its complexity, has always been a subject of controversy. Probably nowhere is this more true than in those theories centered around the structural history of the Valley and Ridge province of the Appalachians (Figure 1), which is characterized by folded and thrust-faulted, but generally unmetamorphosed, sedimentary rocks. The Paleozoic from the Cambrian to the Pennsylvanian is represented in this province and occurs in thicknesses that total about nine to twelve km (King, 1950).

During the past half century, two major schools of thought have developed regarding the mechanics of deformation of the Valley and Ridge sediments. One of these, the décollement or no-basement-involvement hypothesis, postulates thrust faults along incompetent beds of shale or evaporites which merge at depth with a master sole fault. The involvement of the basement with the deformation is insignificant in this hypothesis. The other hypothesis states that the basement has been the dominant influence on Valley and Ridge structure and that the surface folds and faults reflect tectonic activity in the basement. In discussing the evolution of the modes of thought on Appalachian structure, John Rodgers (1949) called these the "thin-skinned" and "thick-skinned" hypotheses, respectively.

The décollement hypothesis has generally found more support and is championed by many prominent geologists, among whom are

1
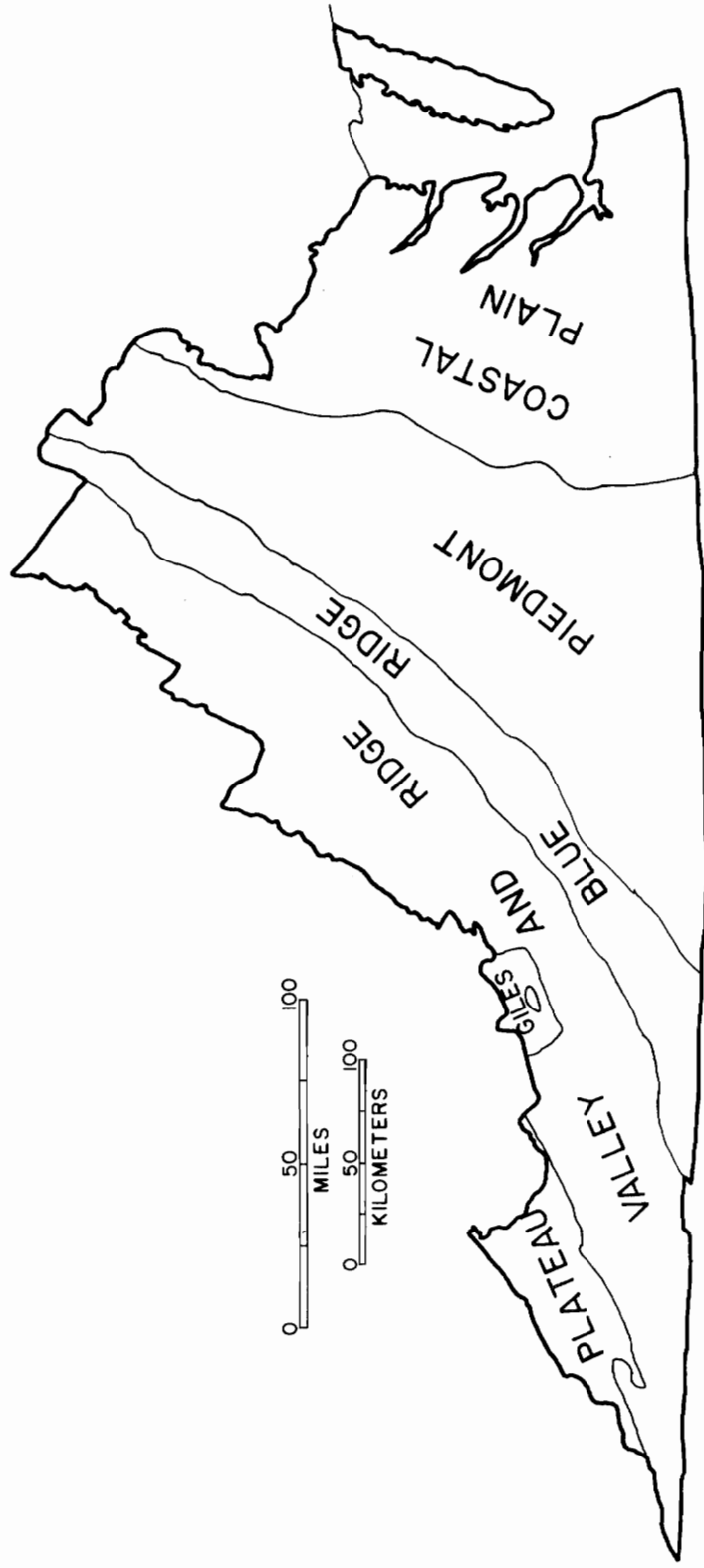
Figure 1. Geologic provinces of Virginia.

Gwinn (1964), King (1950, 1964), Miller (1945), and Rodgers (1949, 1953, 1964). In defense of basement-involvement are B. N. Cooper (1961, 1964, 1968, 1971) and Lowry (1957).

Both hypotheses are supported by good evidence on a regional basis and in specific areas, which led Rodgers (1953) to conclude:

> . . . proof [of the correctness of either hypothesis] is not yet forthcoming. Perhaps it can be obtained by further geologic mapping or by detailed geophysical work, either magnetic or seismic, or perhaps it can be obtained only by drilling.

Unfortunately, as King (1964) points out:

> Our trouble is that we possess an embarrassing richness of information on the surface rocks, and an embarrassing poverty of information on the rocks beneath the surface. Hence, most of our speculations and reconstructions have been based on surface data, supplemented in a few places by the records of drill holes.

The Bane Dome, a doubly-plunging anticline in Giles County, Virginia (outlined area in Figure 1), may be a critical structure for both theories. Along with the Burkes Garden Dome, it is the structurally high part of the folded Appalachians in this part of Virginia northwest of the overthrust belt. The oval area outlined in Giles County in Figure 1 represents outcropping Cambrian formations of Rome shale, Honaker dolomite, and Nolichucky shale. The axis of the anticline strikes approximately N 70° E, and Rome shale crops out in the core of the dome on Virginia State Route 100, about eight km south of Pearisburg. In 1948 the Strader Test Well #1 was drilled by the California Company to a depth of 418 meters

at a site located on the Rome shale. Since everywhere else in
southwest Virginia the Rome shale was bordered on one side by a
thrust fault, "thin-skinned" geology predicted that here the Rome
would be very thick and would overlie a sequence of younger Paleo-
zoic rock, possibly as young as Devonian. The well showed other-
wise; it drilled through only about nine meters of Rome shale. In
fact, the entire Rome at Bane is only about 107 meters thick, and
most of that is exposed. Even more surprising than the thinness
of the shale was the fact that it was underlain by what appears to
be Shady dolomite. The well bottomed in a welded quartzite that
may be the Erwin, the uppermost unit in the Lower Cambrian Chil-
howee Group (Cooper, 1971). If a master thrust fault exists in the
Valley and Ridge, it must also pass under the Bane Dome, according
to décollement theory. The most likely place for the fault would
be in the Rome shale, but it is not there, as the test well showed.
In fact, this event was the beginning of Cooper's disenchantment
with "thin-skinned" geology (Cooper, 1964). Any thrust fault pass-
ing under the Bane anticline must then be in a lower unit. Other-
wise, serious consideration must be given to the "thick-skinned"
interpretation that the Bane Dome is an "ordinary" anticline caused
by upwarping in the basement and that the basement has had a sig-
nificant effect on Valley and Ridge tectonics, since the Bane Dome
is one of the largest topographic features in this part of Virginia.
If this is so, the depth to basement beneath this structure must be
less than it would be if a repeated sedimentary section were pres-

ent. Cooper (1968) sums up the problem and the significance of the Bane Dome when he says:

> . . . the Bane anticline looms as a particularly
> fine location for settling the controversy over
> the nature and cause of Appalachian deformation.

With the thoughts of Rodgers, King, and Cooper in mind, a seismic reflection study was undertaken to try to determine the depth to the basement under the Bane Dome. If successful, it was hoped that this information would shed some light on the problem, or at least add fuel to the controversy.

At first it was hoped that a suitable location for a geophone spread could be found on the Rome shale, but this was not the case. The site that was finally chosen was an undeveloped dirt road between Rye Valley and Guinea Mountain in the lower center of the Pearisburg, Virginia, 7½-minute topographic map. This road had the advantage of being along the strike of the anticline and near its crest, as well as being near a source of water, Walker Creek, which was needed for drilling the shotholes. This location had a major disadvantage in that it involved difficult drilling in Honaker dolomite.

FIELD PROCEDURE

From mid-July to early September 1972 eleven shotholes were drilled by the side of an unimproved road between Rye Valley and Guinea Mountain. Drilling was done with a Mayhew 500 truck-mounted rotary drill and mud pump; hole depths ranged from 10.7 to 18.3 meters. Normally, to minimize the generation of surface waves, it is desirable to drill to depths greater than thirty meters for each shothole, but serious problems were encountered when drilling in the Honaker dolomite. Aside from being extremely hard, which meant slow drilling, the dolomite was fractured in places, which resulted in the pipe string often becoming stuck in the hole; more serious than this was the frequent loss of water circulation.

A spread consisting of three lengths of cable, each having twelve geophone take-outs, was laid out in the configuration shown in Figure 2, which also shows the relative positions of the shot-points. The overall length of the spread was about one kilometer. To each take-out was clipped a closely-clustered group of six geophones, each having a natural frequency of 29 Hz. No attempt was made to spread the phones out in an array to cancel surface waves. Recording was done with a truck-mounted 40-channel seismic recording system capable of making paper (photographic) and magnetic records simultaneously. The system also had the capability of playing back the analog tapes in the field to check the effects of various instrument settings.

6

Figure 2. Shotpoint – geophone configuration
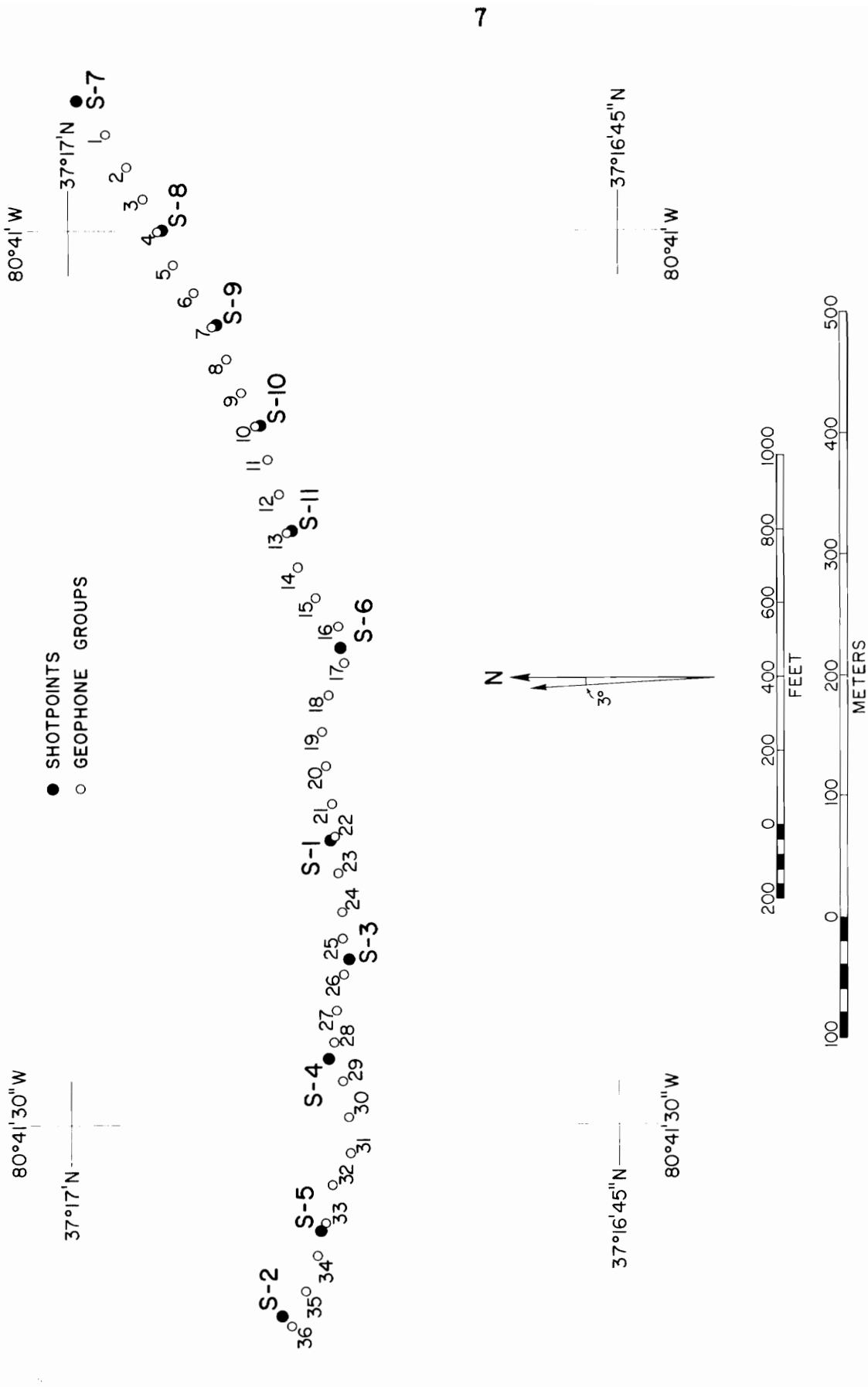
Each hole was loaded with a 20-pound charge of ammonium nitrate blasting agent. Table 1 shows the depths of the charges, the instrument settings, dates that the holes were shot, and other relevant comments. Energy coupling was usually less than ideal, since some shotholes bottomed in caves, while others cratered upon detonation. Eleven records of varying quality were obtained.

TABLE 1

BECORDING PARAMETERS

SHOTPOINT	RECORD	ANALOG TAPE No.	DATE	CHARGE DEPTH (Meters) TOP	BOTTOM	AVC*	EXP#	EG†	FG†	HI-LINE**	FREQUENCY FILTER PASSBAND (Hz)##	COMMENTS
1	BANE 1-1	1382069	7-28-72	11.0	14.0	ON	OFF	8	8	IN	12 – 50	BANE 1-1 and 1-2 shot in heavy rain
2	BANE 1-2	1382169	7-28-72	13.1	16.2	ON	OFF	8	8	IN	12 – 50	
3	BANE 2-1	1382369	8-22-72	7.6	10.7	OFF	ON	8	10	OUT	12 – 62	Bottomed in cave
4	BANE 2-2	1382469	8-22-72	10.7	13.7	ON	ON	7	10	OUT	12 – 62	Combined AVC and EXP accidentally used for shots 2-2 and 2-3
5	BANE 2-3	1382569	8-22-72	7.3	10.4	ON	ON	7	10	OUT	12 – 62	
6	BANE 2-4	1387469	8-22-72	9.8	12.8	OFF	ON	7	10	OUT	12 – 62	EXP rate 9 for shots 2-1 through 2-4
7	BANE 3-1	1387369	9-7-72	12.2	15.2	OFF	ON	6	10	OUT	12 – 62	Shot in sequence 3-1,3-2,3-4,3-5,3-3
8	BANE 3-2	1387269	9-7-72	7.9	11.0	OFF	ON	6	10	OUT	12 – 62	
9	BANE 3-3	1386969	9-7-72	2.7	5.8	OFF	ON	6	10	OUT	12 – 62	Charge in weathered layer***
10	BANE 3-4	1387169	9-7-72	7.6	10.7	OFF	ON	6	10	OUT	12 – 62	Bottomed in cave
11	BANE 3-5	1387069	9-7-72	9.1	12.2	OFF	ON	6	10	OUT	12 – 62	Hole cratered; lost uphole phone. EXP rate 6 for 3-1 through 3-5 (all five)

*** Blockage in hole, so charge was shallow. Used trace 7 for uphole time because uphole phone lost on 3-5.

* AVC = AGC; Automatic Gain Control

EXP = Expander; increases signal gain at a constant rate

† EG and FG = Early gain and final gain; expander parameters

** HI-LINE — Eliminates multiples of 60-Hz electrical noise

Passband cutoffs for 6 db attenuation

DATA PROCESSING

The analog magnetic tapes were digitized and transferred to computer tape by GTS Corporation and by the Amoco Production Co., using a digitizing interval of 2 ms. Digitization was started at the tape head pulses rather than at the time breaks. This made necessary the application of datum corrections in order to begin the processing at the time breaks. These datum corrections ranged from 153 to 880 ms.

Frequency filtering

Surface waves are a common type of "noise" in exploration
seismology that interferes with reflected energy. Other sources
of noise are wind, streams, and 60-cycle electrical energy.
Since the reflected energy of interest has a characteristic
frequency range, frequency filtering can often be used to elim-
inate some of the noise while retaining the desired reflected
signal. The filter can be electronic or digital or both. In this
study all electronic filtering was done in the field, usually with a
passband of 12 to 62 Hz, except for the first two seismograms which
were obtained during a heavy rain. The upper cutoff for these
shots was 50 Hz in order to attenuate the severe 60-cycle noise
associated with wet conditions (see Table 1). For all other
records, an electronic notch filter designed to eliminate elec-
trical noise was also used.

Digital filtering was done by taking the Fourier transform of
a seismic trace, multiplying it by a passband filter designed in
the frequency domain (Bogert, 1962), and then transforming the
filtered trace back into the time domain. In this manner an entire
seismic record could be frequency-filtered one trace at a time.
The filtering was done using the fast Fourier transform (Cooley
and Tukey, 1965; Robinson, 1967).

By itself, frequency filtering did not produce impressive
results. Figures 3 and 4 show portions of records #2 (Bane 1-2) and
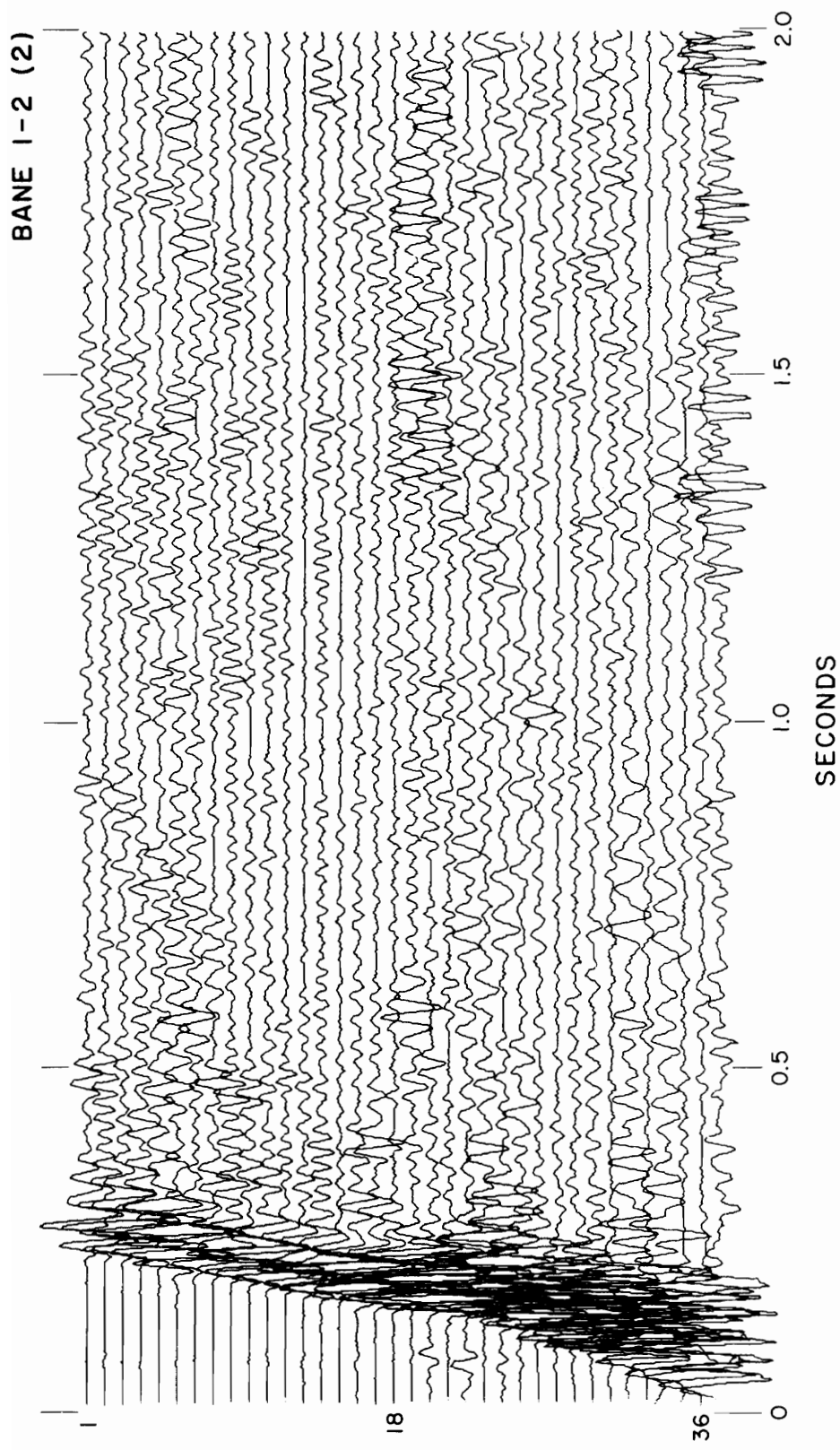
Figure 3. Bane I-2 (Shotpoint 2). Electronically filtered only.
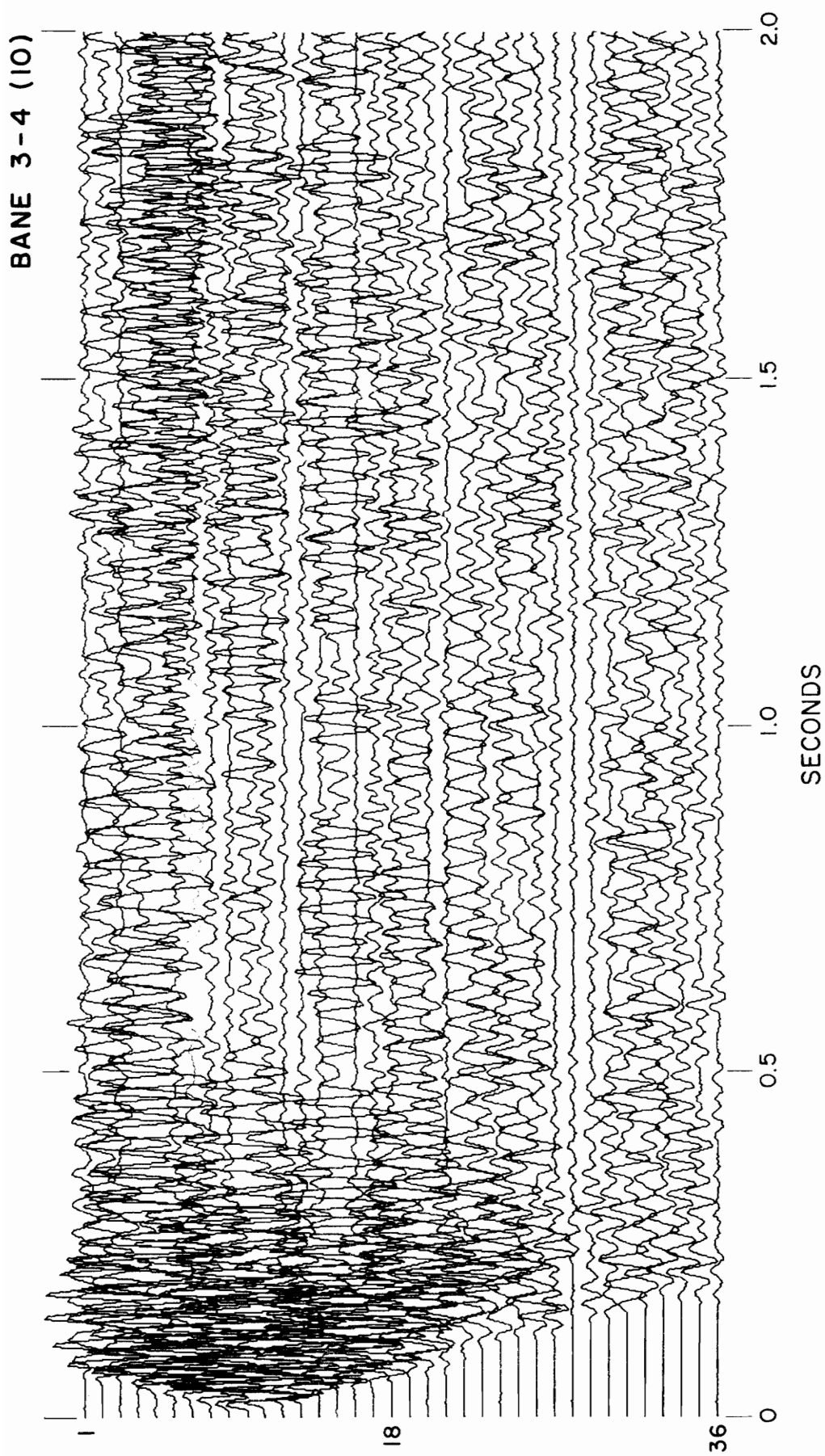
Figure 4. Bane 3-4 (Shotpoint 10). Electronically filtered only.

#10 (Bane 3-4), respectively, that have been electronically fil-
tered when recorded, but have not been filtered digitally.
Figures 5 and 6 show the same two records after digital filtering
using a passband filter down 6 db at 27.5 and 54.0 Hz. The records
are better, but it is still not possible to discern any reflected
events by visual examination. Processing methods other than
frequency filtering were more effective in enhancing the data.
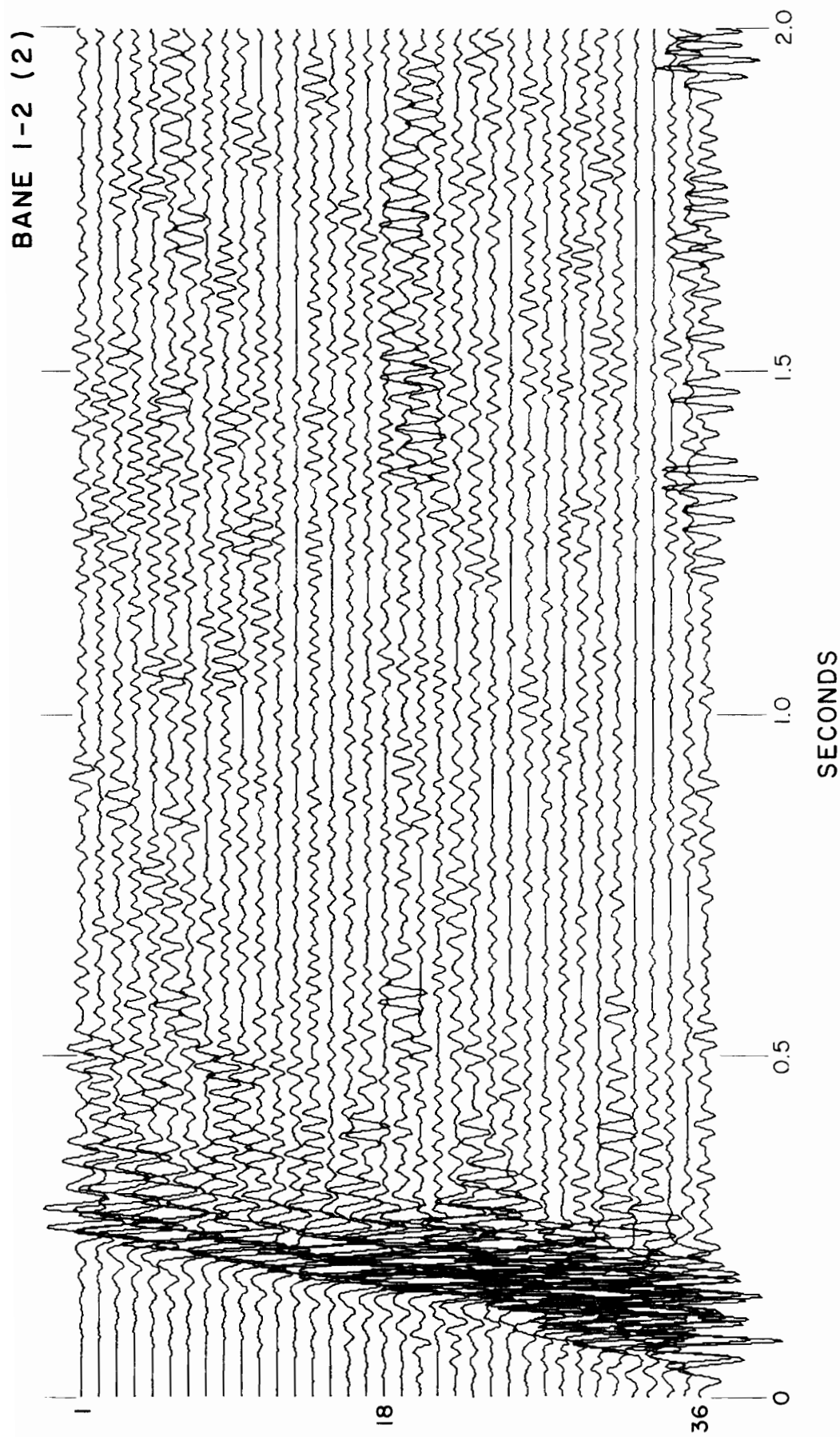
Figure 5.   Bane 1-2.   After digital frequency filtering.
Filter passband: 28 - 54 Hz.
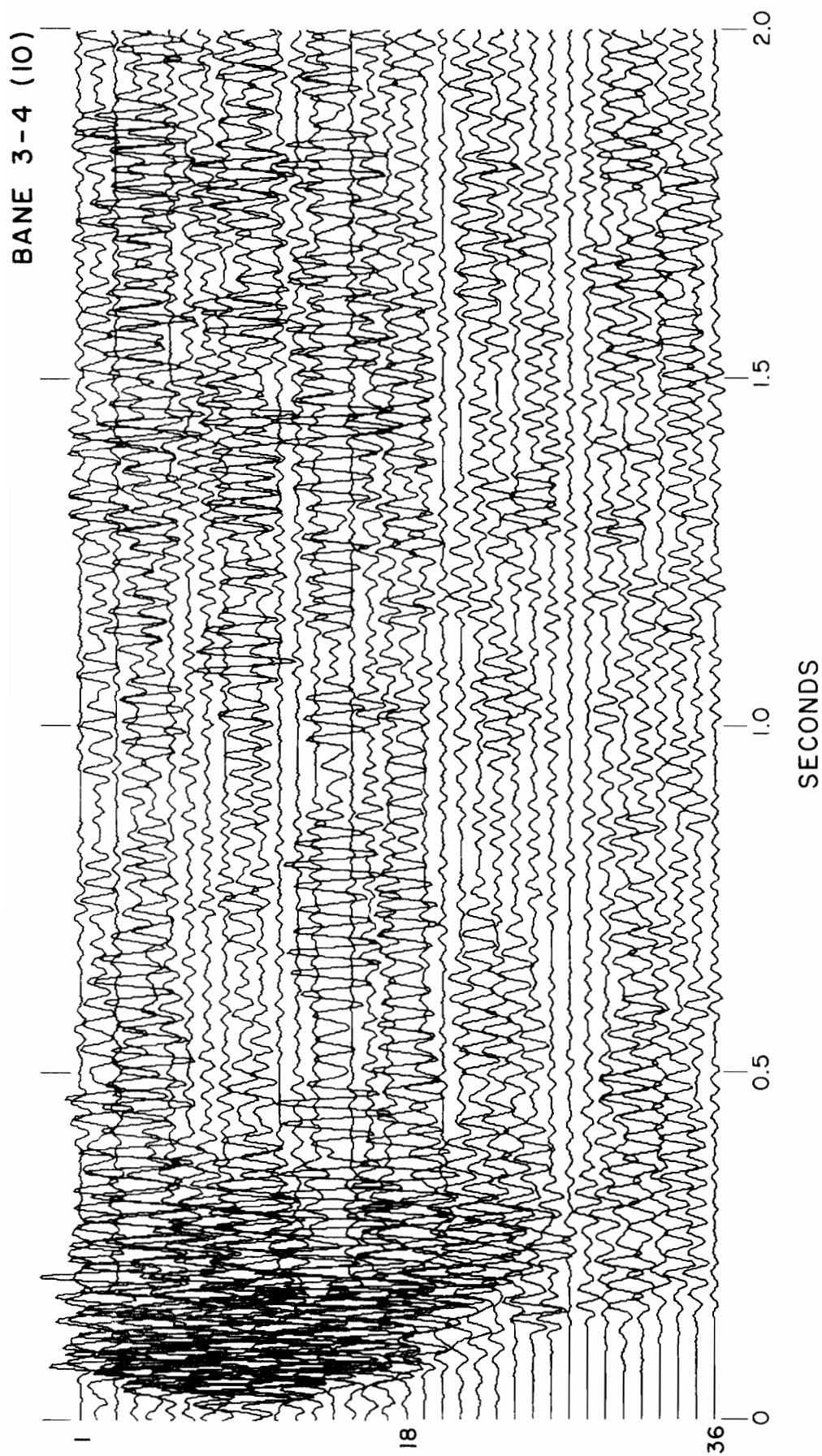
Figure 6. Bane 3-4. After digital frequency filtering.
Filter passband: 28 – 54 Hz.

RMS velocity analysis

Since it is often difficult or impossible to pick reflection arrival times accurately by visual inspection of a seismogram, a method has been developed (Taner and Koehler, 1969) that scans the record with a "window" that tracks a hyperbolic path defined by

$$T_{x,n}^2 = T_{0,n}^2 + \frac{x^2}{\bar{V}_n^2}$$

where $T_{x,n}$ is the total slant-path traveltime to the base of the nth layer, $T_{0,n}$ is the vertical two-way traveltime to the reflector, x is the shotpoint-geophone distance, and $\bar{V}_n$ is the "RMS velocity" to the reflector. Since there are generally several reflecting interfaces, each separating different interval velocities, the scanning velocity, $\bar{V}_n$, used to track the reflecting wavelet from the base of the nth layer is actually a time-weighted, mean-square velocity given by (Taner and Koehler, 1969, eq. (7)):

$$\bar{V}_n^2 = \frac{\sum_{k=1}^{n} v_k^2 t_k}{T_{0,n}}$$

where t_k is the two-way traveltime within the kth layer. The interval velocity, v_k, can be recovered from the above equation by picking values of $\bar{V}_n$ and $T_{0,n}$ from the velocity analysis (Dix, 1955).

If the scanning window follows the reflected wavelet correctly, the signals tracked from trace to trace will show a high degree of correlation; if an incorrect hyperbola is assumed, the adjacent traces will have a lower degree of correlation. Correlation coefficients were obtained for a range of velocities and times and plotted as a contour map. Closed contours around high coefficient values indicate a coherent event.

Figure 7a is the plot resulting from a hyperbolic scan of Bane 1-2. The window was shifted down the record in increments of 40 ms. It would appear that separate events can be identified at A, B, C, D, E, and F. These are examples of the phenomenon described by Costain and Robinson (1972) that occurs as a result of the finite width of the scanning window and the finite length of the seismic source wavelet. If the window is, say, 100 ms wide and the wavelet is about 300 ms long, then several possibilities exist for obtaining high values of the semblance coefficient. If the window tracks the normal moveout of the wavelet as shown for window A in Figure 8, then a high value of the semblance coeffi_ cient will result, even though the window is at an incorrect record T_0-time. In order to line up the reflected event in the window using the value of T_0 associated with the window as shown in Figure 8, it is necessary to use an incorrect (higher) value of $\bar{V}$. It is only when the T_0 of the window coincides with the correct arrival time of the reflected wavelet that the reflection will be flattened by the correct RMS velocity. High semblance coefficients
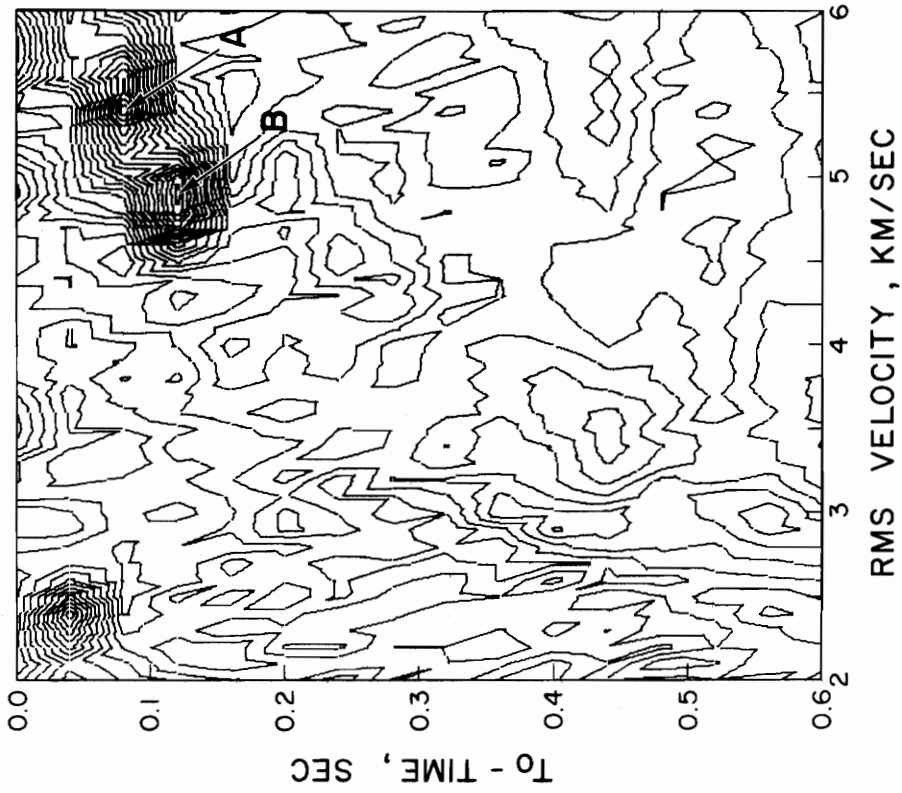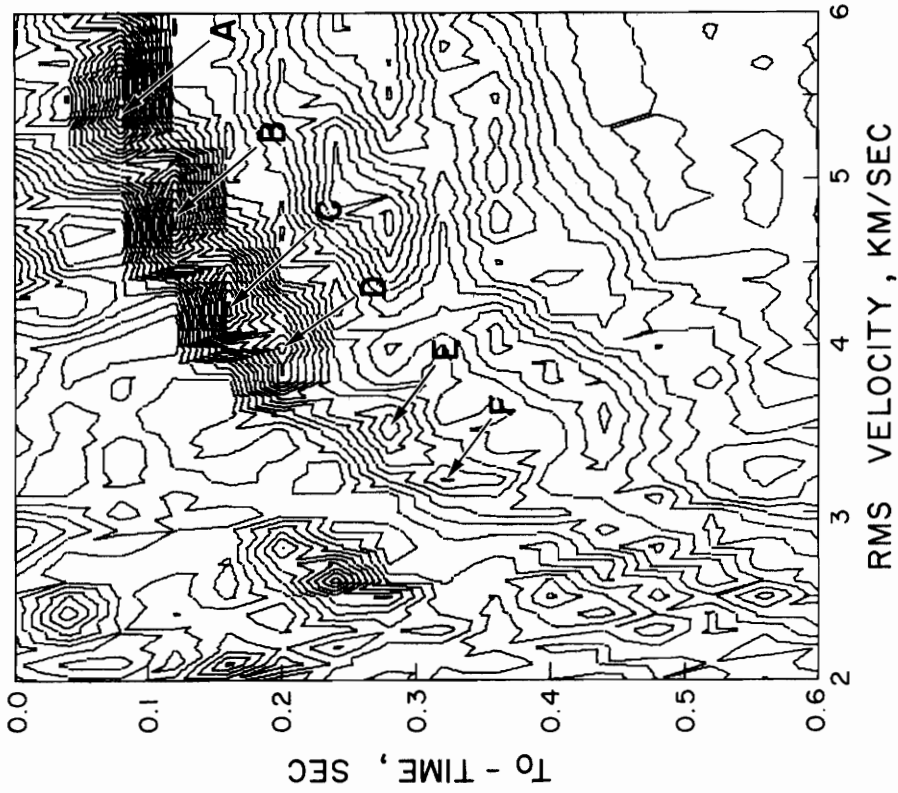
Figure 7. Velocity analyses of Bane 1-2. Filter: 28 - 54 Hz.

a. Not deconvolved

b. Deconvolved
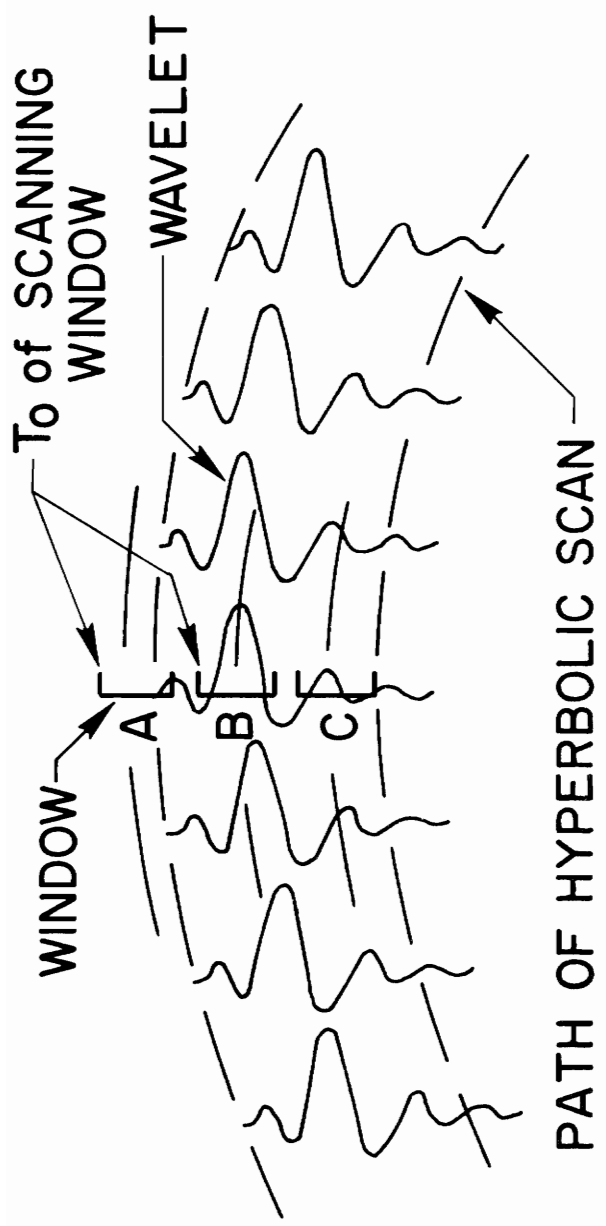
Figure 8. Relationship between hyperbolic scan, To of scanning window, and length of source wavelet.

will also be obtained for windows B and C which track the same
wavelet at the same normal moveout, but using different T_0-times.
The normal moveout is thus the same at several T_0-times, resulting
in several different RMS velocities for the same source wavelet.
This is manifested by a characteristic pattern of closed contours
on a plot of the semblance coefficients.

Normal moveout is given by the expression:

$$NMO = T - T_0 = (T_0^2 + \frac{x^2}{\overline{V}^2})^{\frac{1}{2}} - T_0$$

where T is the slant-path traveltime, T_0 is the vertical two-way
traveltime, x is the shotpoint-geophone distance, and $\overline{V}$ is the
RMS velocity associated with the reflected event.

If the normal moveout is the same for all six "events,"
A, B, C, D, E, and F, in Figure 7a, then it follows that

$$(T_{0_A}^2 + \frac{x^2}{\overline{V}_A^2})^{\frac{1}{2}} - T_{0_A} = (T_{0_B}^2 + \frac{x^2}{\overline{V}_B^2})^{\frac{1}{2}} - T_{0_B} = \cdots$$

that is, $(T_0^2 + \frac{x^2}{\overline{V}^2})^{\frac{1}{2}} - T_0 = $ Constant

By substituting values of T_0 and $\overline{V}$, this relationship can be used
to test the validity of picks made from a contoured velocity
analysis. The greatest value of x for a given seismogram is
chosen, since this is where the normal moveout is most pronounced.

If two or more events all satisfy the above relationship, they probably do not all represent real reflections (Costain and Robinson, 1972).

Applying the above relationship to the T_0-times and RMS velocities at A, B, C, D, E, and F gives

$$0.1217 \doteq 0.1204 \doteq 0.1268 \doteq 0.1202 \doteq 0.1261 \doteq 0.1272$$

These six values agree within about six percent with the average value of 0.1237, indicating that a single reflection is responsible for all six "events."

If all six events are associated with the same source wavelet, then a long wavelet must be involved. This will be the case if the wavelet is reverberating. Examination of the autocorrelation functions of traces confirmed that the source wavelets are indeed of long time duration and that reverberations are present. Predictive deconvolution was sometimes successful in shortening the reverberating source pulse, thereby increasing the resolution on the seismogram. As shown by a comparison of Figures 7a and 7b, several of the peaks in the RMS velocity analysis were effectively removed by deconvolution, supporting the interpretation that correlation highs at C, D, E, and F are associated with a reverberating source wavelet. In the example of Figure 7a, the separation of the contours into events at A, B, C, D, E, and F is simply a consequence of using a relatively large window shift increment of 40 ms.

Deconvolution was not always successful in shortening the length of a reverberating wavelet. Interference by surface waves made an accurate estimation of the autocorrelation function of the reflected energy difficult or impossible. Attempts to obtain the autocorrelation function at later record times and use this to design a deconvolution filter for the early part of the record were not always successful, indicating that the entire seismic trace was not a stationary time series. Event B in Figure 7b remains after deconvolution simply because the autocorrelation function of the seismic wavelet is difficult to estimate accurately in the presence of noise such as surface waves. Event B could very probably have been removed or attenuated with a different prediction distance when the deconvolution filter was designed, or by different approaches to determining the autocorrelation of the seismic wavelet.

The characteristic pattern of a reflected reverberating wavelet on a contoured velocity analysis is actually helpful in confirming the identification of a reflected event. The correct values of T_0 and $\bar{V}$ can be found by noting the value of T_0 corresponding to the first appearance of coherence defined by the contoured pattern of the reflection. Since the first appearance of correlation on the contour plot must mean that the leading edge of the wavelet is just beginning to appear in the window, then the width of the scanning window must be added to the value of T_0 at which coherence first appears on the contoured velocity analysis. The correct value of

$\bar{V}$ is obtained by observing the maximum semblance value corresponding to this value of T_0.

Some allowance may also have to be made for the scanning shift increment. For example, if the window is shifted down the record in increments of 0.01 second, the window may actually be 0.01 second into the wavelet when the first semblance appears. In this case the T_0-time is corrected by adding the width of the window to the T_0-time indicated and subtracting one scanning increment. Since it is difficult to determine exactly when the first semblance appears, and since it is impossible to know where the wavelet is in the window, some uncertainty exists when picking T_0 and $\bar{V}$. A study of synthetic data showed that the onset of the appearance of correlation depends on the rise time of the first motion of the reverberating wavelet. For a wavelet with its highest amplitude at the first half-cycle of the wavelet, the first appearance of coherence on the contoured velocity analysis is sharp and unambiguous, resulting in an accurate determination of T_0 and $\bar{V}$.

Figures 9 and 10 show the effects on a velocity analysis of the shape of the reflected wavelet and the width of the scanning window. The velocity analyses were derived from the synthetic seismograms shown in Figure 11. It is apparent that if the wavelet is impulsive instead of emergent, the contoured correlation pattern will also be impulsive rather than emergent. The results of the synthetic study suggest that significant information about the energy distribution and duration of the source wavelet is contained
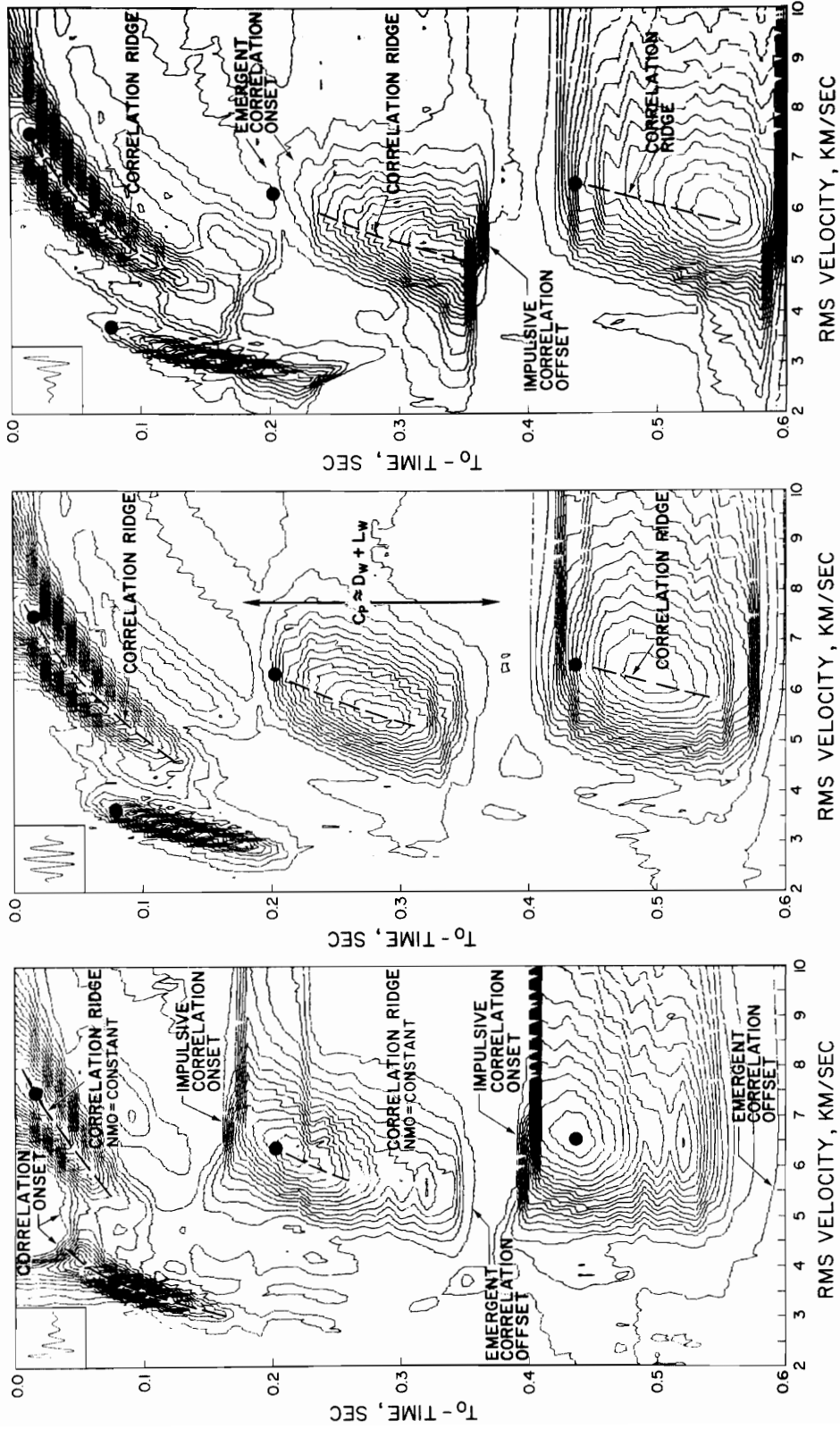
Figure 9. Velocity analyses of synthetic data for different source wavelets and a scanning window of 50ms.
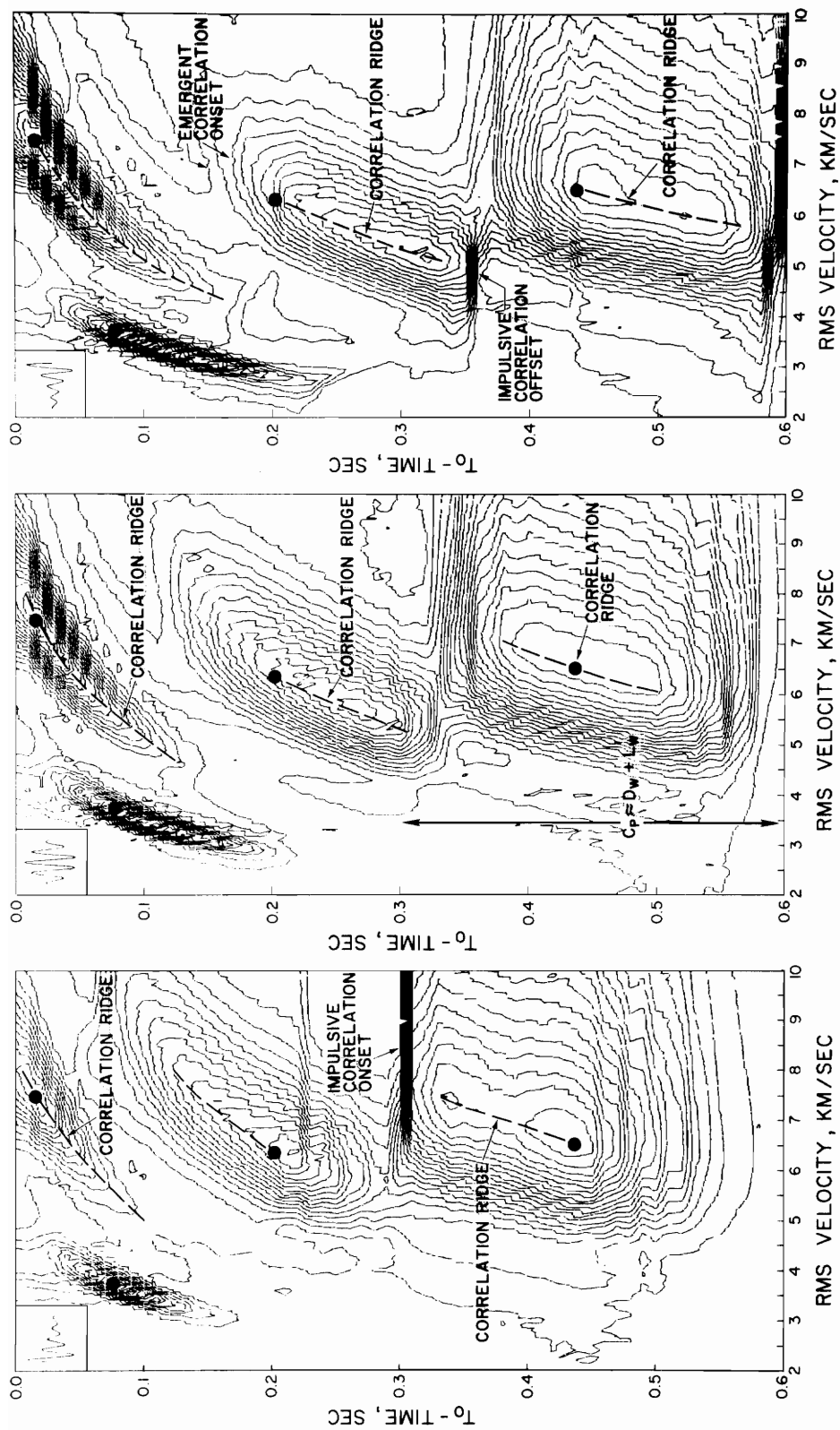
Figure 10. Velocity analyses of synthetic data for different source wavelets and a scanning window of 150 ms.
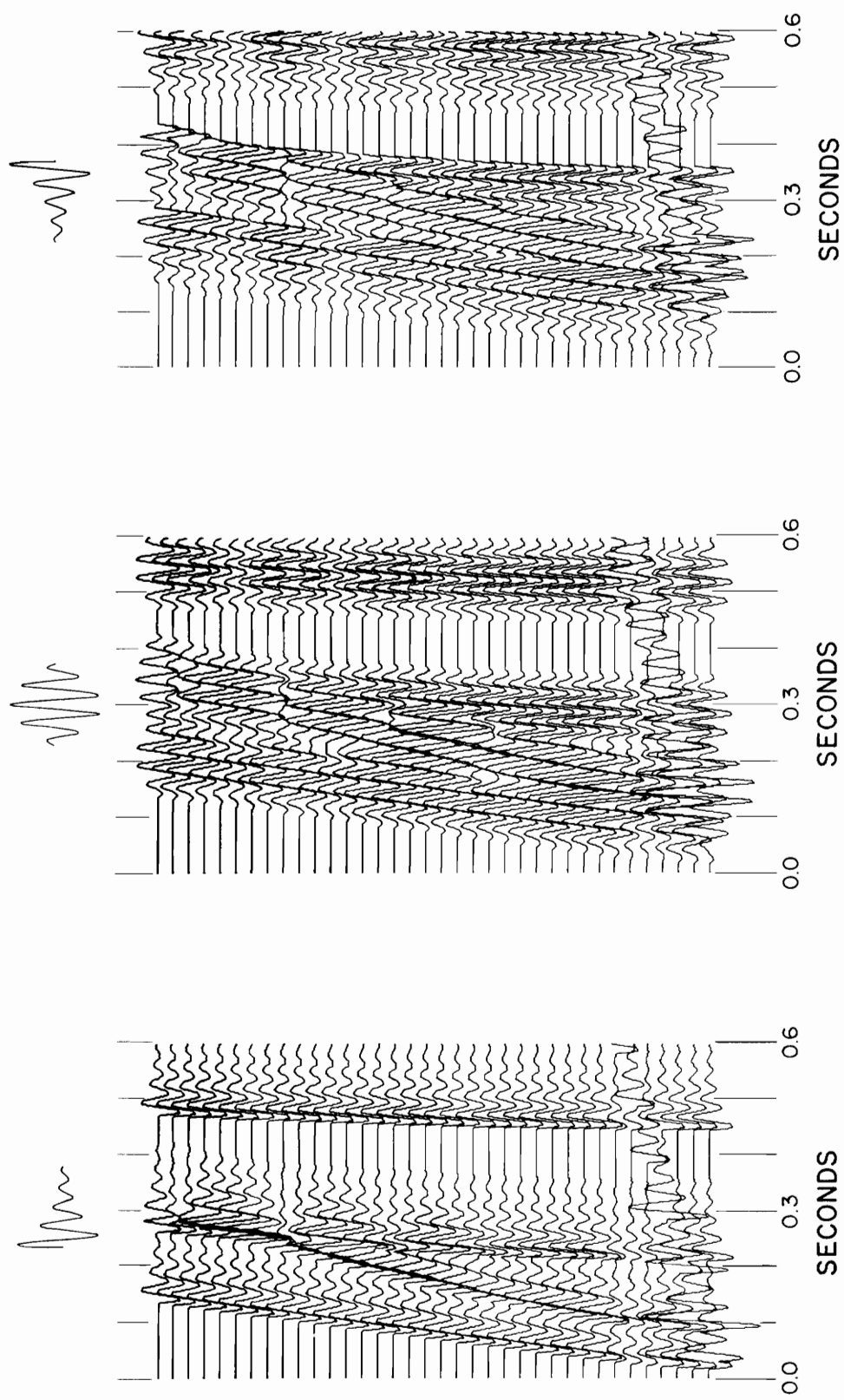
Figure II.   Synthetic seismograms used for velocity scans of Figures 9 and IO.

in a velocity analysis. Indeed, the length of the wavelet, L_W,
is related to the time-duration of the contoured correlation
pattern, C_p, and the window, D_W, by

$$C_p = D_W + L_W$$

Predictive deconvolution

Signal energy recorded on a seismogram consists of overlapping reflected source wavelets which, if they are excessively long, will interfere with each other, are detrimental to resolution, and make the seismogram complicated and difficult to interpret. Predictive deconvolution allows one to control the length of the desired source wavelet, and hence to specify the desired degree of resolution. The method is effective in the suppression of rather complex reverberation patterns (Peacock and Treitel, 1969; Robinson, 1967).

Predictive deconvolution is often useful in increasing resolution where reverberations are introduced into the seismogram as a result of a low-velocity weathered layer overlying consolidated rock of a higher velocity, producing reverberations similar to those caused by a water layer in marine seismology. That there was, in fact, a problem with reverberations can be seen by examining the autocorrelations shown in Figure 12, which also shows the frequency spectra of trace 10 of record #1 (Bane 1-1) before and after deconvolution.

The appearance of the autocorrelation after deconvolution is often used to evaluate the effectiveness of the process. It is clear, however, that the autocorrelation function cannot always be used to evaluate the effectiveness of deconvolution. The least squares filter used for any deconvolution is specifically designed to give a filtered trace whose autocorrelation must be close to
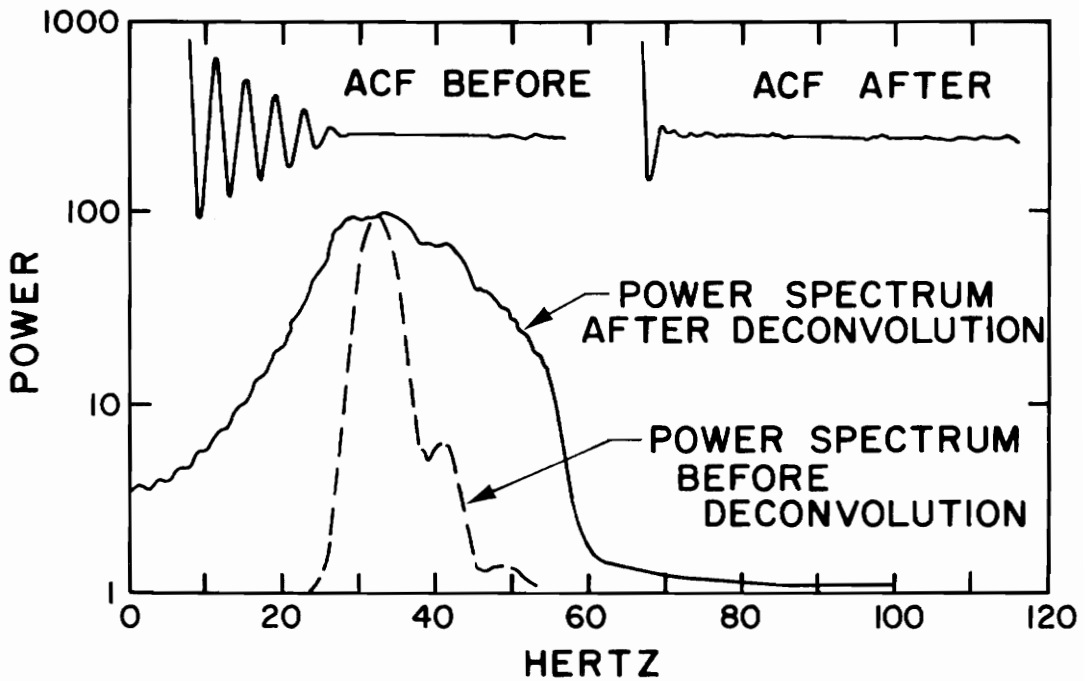
Figure 12. Bane 1-1, Trace 10. Power spectra and autocorrelation functions before and after deconvolution.

zero after some specified prediction distance. No assumption whatever is made with regard to how accurately the autocorrelation of the seismic trace represents the autocorrelation of the actual source wavelet, which it will certainly not do if the seismic trace does not represent a stationary time series. Deconvolution was not particularly useful in enhancing the data in the present study because of the presence of surface wave noise which precluded obtaining an accurate autocorrelation function.

Velocity filtering

Velocity filtering is a multichannel operation which makes
use of the fact that some types of noise and most desired signals
exhibit distinct ranges of apparent velocities on seismograms.
The principles behind the filter are described by Embree and
others (1963), whose work parallels that done independently and
published earlier by Fail and Grau (1963).

Velocity filtering makes it possible to process a seismogram
in such a way that all seismic events with apparent velocities
within a given range are preserved with no distortion over a wide
frequency band, while all seismic events with apparent velocities
outside the specified range are uniformly and severely attenuated.
By applying this process to a noisy seismogram, a filtered record
may be obtained which has all events within a specified velocity
range perfectly preserved and events outside of this range essen-
tially eliminated, a result which is impossible by frequency fil-
tering or conventional array usage. In structurally complex areas
where several events interfere, the technique may be applied to
separate events with different apparent velocities. In areas where
a normal moveout difference exists between primaries and multiples,
the technique may be used for wide-band multiple attenuation (Embree
and others, 1963).

An unprocessed portion of record #1 (Bane 1-1) is shown in
Figure 13. Figure 14 shows the same record after frequency and
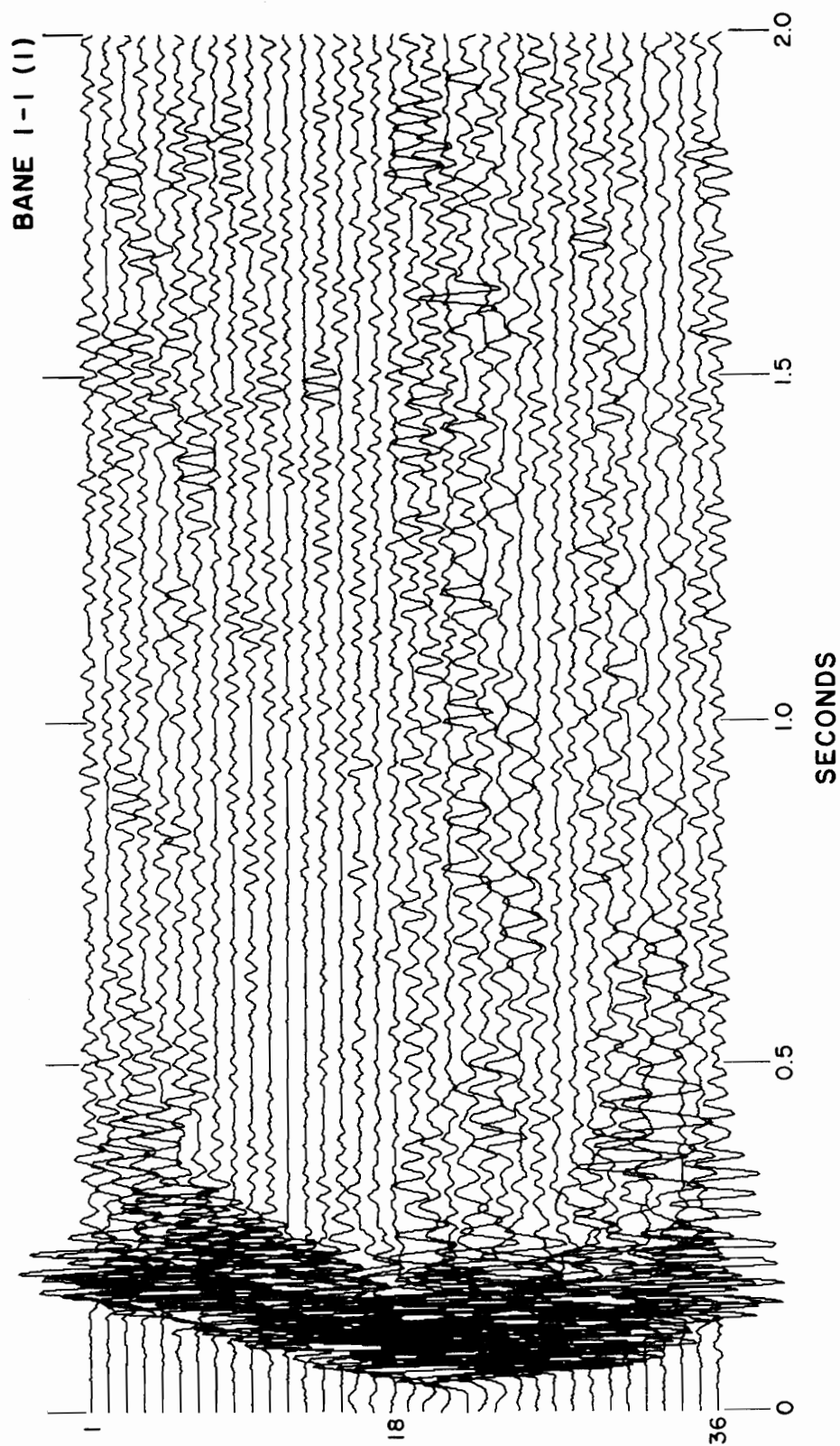
Figure 13. Bane I-I (Shotpoint I). Electronically filtered.
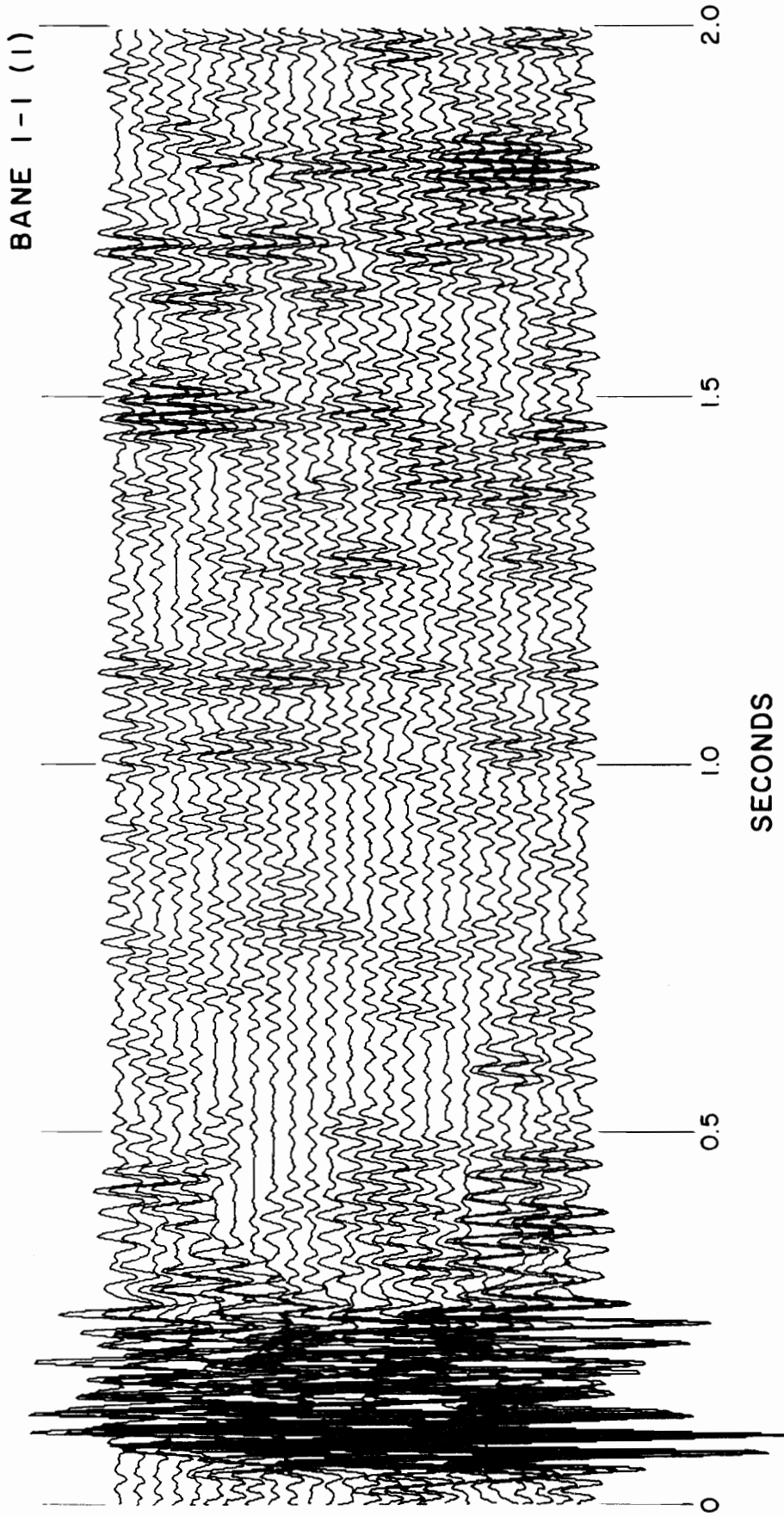
Figure 14. Bane 1-1. Velocity – filtered .
Beam direction = 0 ms/trace ;
velocity passband = ±2 ms/trace .
Frequency filter = 28 –54 Hz .

velocity filtering. Two events at about 1.0 and 1.1 seconds can be discerned. Figure 15, a velocity filtered section of record #2 (Bane 1-2), shows a strong reflection at 1.05 seconds.
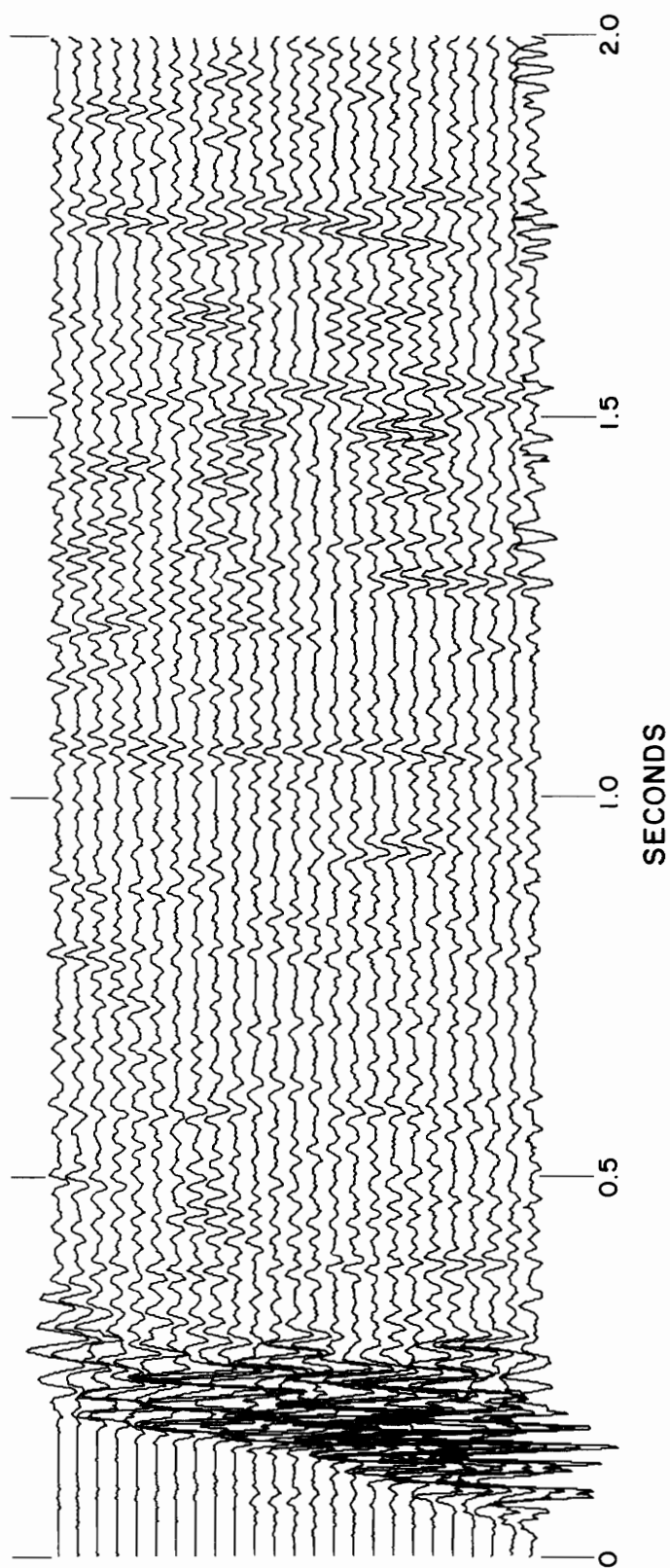
Figure 15. Bane 1-2. Velocity-filtered. Beam direction = 0 ms/trace; velocity passband = ±2 ms/trace.

SECONDS

INTERPRETATION

Interpretation of the data was aided by assuming models of the
stratigraphic section. The thickness of the Honaker dolomite is
known to be about 400 meters in the area of the Bane Dome (Cooper,
1961). Based on Cooper's estimates and the Strader well (Cooper,
1964, 1968), the thicknesses of the Rome shale and Shady dolomite
at the Bane Dome should be approximately 105 and 390 meters,
respectively. The nearest measured Cambrian section of Unicoi
sandstone, Hampton shale, Erwin sandstone, Shady dolomite, and Rome
shale and dolomite is in Wythe and Grayson Counties, approximately
50 to 55 km southwest of Bane. Here the Unicoi is about 670 meters
thick and the Hampton about 365 to 610 meters thick (Cooper, 1961).
Currier (1935) estimates a thickness of 150 to 245 meters for the
Erwin, but Miller (1944) estimates a thickness of 455 to 610 meters
near Glade Mountain in Smyth County. The Shady occurs in thick-
nesses ranging from 305 to 790 meters (Currier, 1935), and the Rome
is 610 to 850 meters thick in these localities (Currier, 1935;
Cooper, 1961).

Ultrasonic velocity measurements were made on rock samples
thought to be representative of the Cambrian sequence and Precam-
brian basement rocks at the Bane anticline. These velocities are
the basis of the interval velocities assumed in the models and are
given in Table 2. A simple three-layer model consisting of Honaker
dolomite, Rome shale, and Shady dolomite was considered first. RMS

37

TABLE 2

Ultrasonic Velocity Measurements
(in km/sec)

Sample	Pressure (Atm) 200	400	600	Sample	Pressure (Atm) 200	400	600
Honaker dol.	7.3	7.3	7.2	Hampton sh.	5.3	5.4	5.4
	7.1	7.1	7.1		5.5	5.5	5.4
	7.4	7.5	7.5				
	7.6	7.6	7.6	Unicoi ss.	6.2	6.2	6.2
Rome sh.	3.4	3.7	4.1		5.7	5.9	6.0
	3.3	3.7	3.8				
	3.4	3.7	3.9	**Precambrian Basement Rocks**			
	3.3	3.6	3.7	Augen gneiss	5.9	6.1	6.2
Rome dol.	7.4	7.4	7.3		5.6	5.8	6.0
	7.4	7.4	7.4	Amphibolite	5.5	5.6	5.7
Shady dol.	6.3	6.7	6.9		5.4	5.6	5.7
	6.1	6.7	6.9	Lynchburg amphibolite	6.0	6.1	6.1
	6.3	6.7	6.9		6.4	6.4	6.4
Shady ls.	7.0	7.0	6.9	Lynchburg gneiss	5.1	5.4	5.4
	6.8	6.8	6.8		5.3	5.5	5.5
Erwin ss.	6.0	6.0	6.0		4.6	4.9	5.0
	6.0	6.1	6.1		4.7	4.9	4.9
	5.1	5.4	5.4				
	5.2	5.3	5.3				

velocities for the units in this model were computed for some
assumed thicknesses and are given in Table 3.

If part of the Honaker is replaced by a weathered layer, the
RMS velocity associated with the Honaker is lowered considerably,
as shown in Table 4. The RMS velocities for the Rome and Shady are
also affected. If a weathered layer is placed on top of the Honaker
in the first model with no thinning of the Honaker, the RMS veloci-
ties are still changed (Table 5). The weathered layer can thus
have a significant effect on the RMS velocities of the other rock
units.

A greater thickness of weathering will result in a greater
lowering of the RMS velocities of the underlying layers. Figures
illustrating this point are presented below for comparison. Fig-
ures 16 and 17, which are RMS velocity scans of actual data, show
two corresponding contour patterns, but in Figure 16 these patterns
have lower RMS velocities associated with them. This is because
the weathered layer was thicker at this shotpoint.

On the basis of RMS velocity scans interpreted by the methods
described in a previous section, determinations of the interval
velocities and thicknesses of the Honaker and Rome formations were
attempted, with some allowance being made for a low-velocity weath-
ered layer in each case. Table 6 shows that the Honaker and Shady
dolomites, which lie above and below the Rome, respectively, in a
normal stratigraphic sequence, have acoustic impedances that are
approximately twice that of the Rome shale. This makes it reason-

TABLE 3

Three-layer Stratigraphic Model

Honaker	30 m
Rome	105 m
Shady	390 m

	INTERVAL VELOCITY (km/sec)	T_0 TIME (sec)	RMS VELOCITY (km/sec)
H	7.3	.008	7.3
R	3.4	.071	4.1
S	6.2	.199	5.5

TABLE 4

Honaker Partially Replaced By Weathering

Weathering	3 m	
Honaker	27 m	
Rome	105 m	
Shady	390 m	

	INTERVAL VELOCITY (km/sec)	T_0 TIME (sec)	RMS VELOCITY (km/sec)
W	0.3	.020	0.3
H	7.3	.027	3.8
R	3.4	.091	3.5
S	6.2	.219	5.3

TABLE 5

Original Model With Weathering Added

Weathering	3 m
Honaker	30 m
Rome	105 m
Shady	390 m

	INTERVAL VELOCITY (km/sec)	T_0 TIME (sec)	RMS VELOCITY (km/sec)
W	0.3	.020	0.3
H	7.3	.028	4.0
R	3.4	.092	3.6
S	6.2	.220	5.3
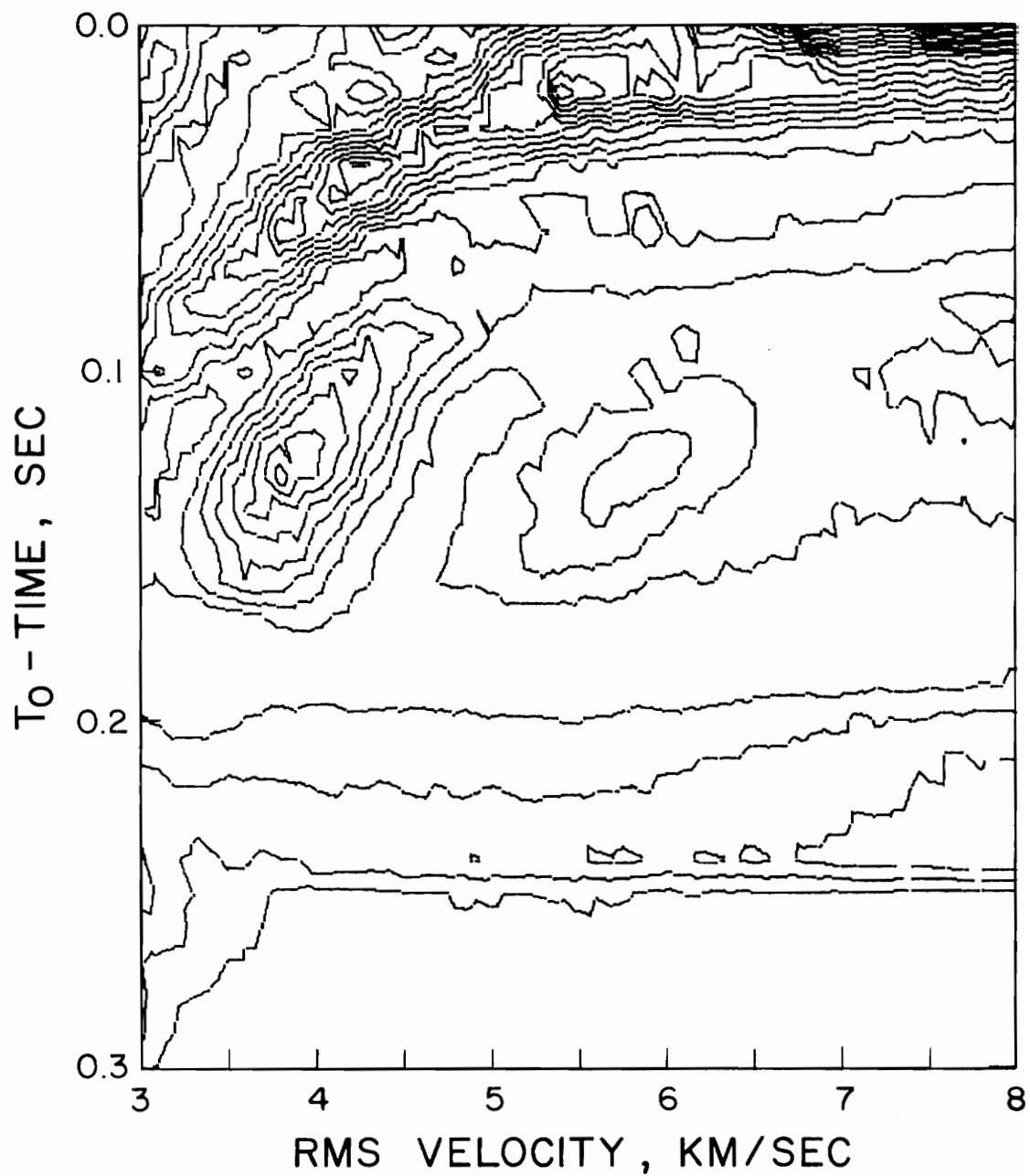
Figure 16. Velocity analysis of Bane 1-1.
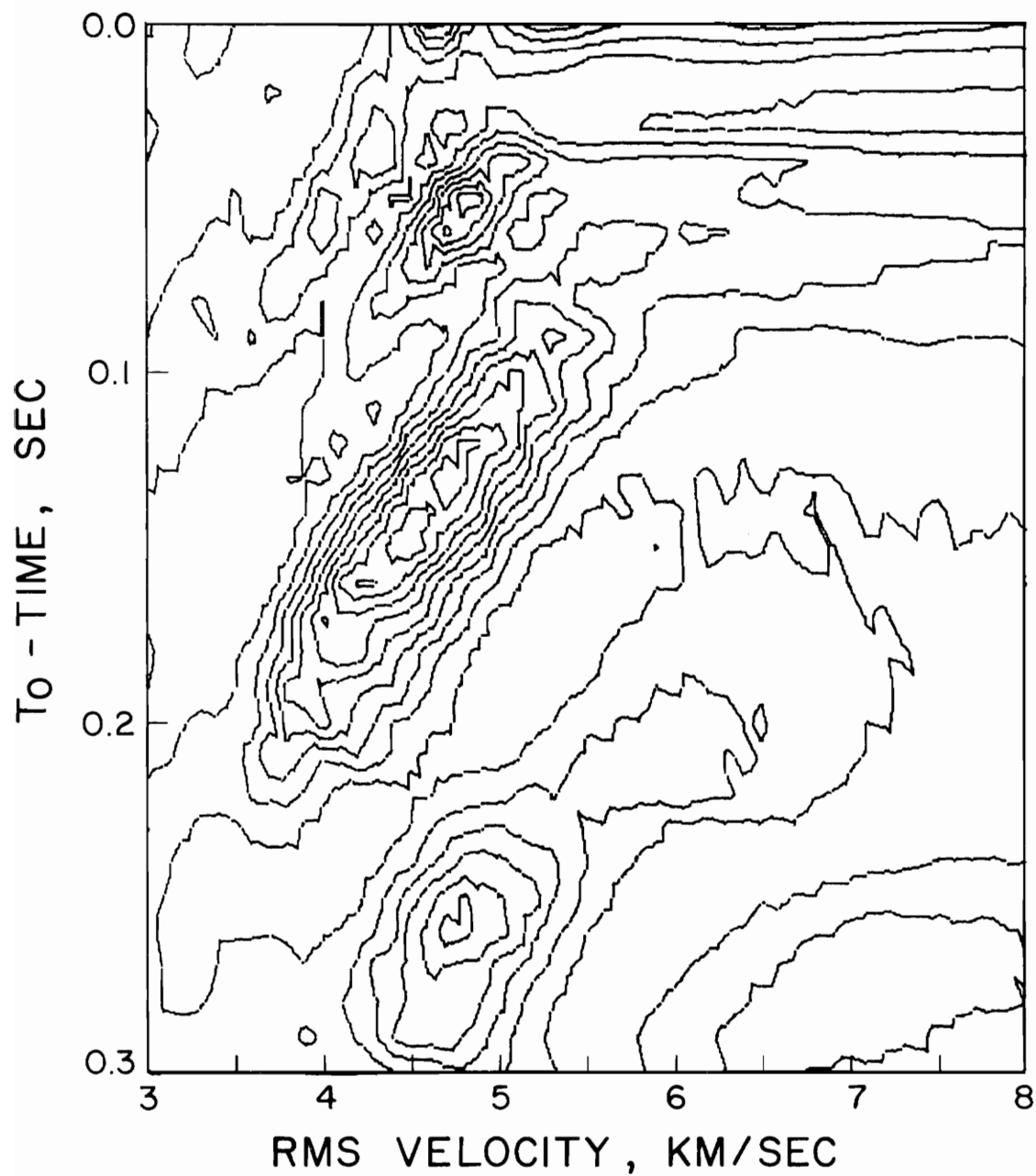
Figure 17. Velocity analysis of Bane 1-2.

TABLE 6

Densities and Acoustic Impedances

Sample	Average Density (gm/cm^3)	Acoustic Impedance (gm/cm^2-sec)
Honaker dol.	2.83	$2.01 \times 10^6 - 2.15 \times 10^6$
Rome sh.	2.67	$0.88 \times 10^6 - 1.09 \times 10^6$
Rome dol.	2.83	$2.06 \times 10^6 - 2.09 \times 10^6$
Shady dol.	2.84	$1.73 \times 10^6 - 1.96 \times 10^6$
Shady ls.	2.73	$1.85 \times 10^6 - 1.91 \times 10^6$
Erwin ss.	2.59	$1.32 \times 10^6 - 1.58 \times 10^6$
Hampton sh.	2.71	$1.43 \times 10^6 - 1.49 \times 10^6$
Unicoi ss.	2.67	$1.52 \times 10^6 - 1.65 \times 10^6$
Augen gn.	2.70	$1.51 \times 10^6 - 1.67 \times 10^6$
Amphibolite	3.00	$1.62 \times 10^6 - 1.71 \times 10^6$
Lynchburg amphibolite	2.97	$1.78 \times 10^6 - 1.90 \times 10^6$
Lynchburg gn.	2.65	$1.22 \times 10^6 - 1.46 \times 10^6$

able to expect that strong reflections from the top and bottom of the Rome should appear as double correlation patterns on the RMS velocity plots. Since the thickness of the Rome is estimated to be on the order of 120 meters at Bane (Whitman, 1964), and since the shotholes were drilled in the lower several hundred feet of Honaker, it may be further expected that the double patterns should appear early in the scan and should be separated by about 70 ms. On six of the scans made of all eleven records, this double pattern could be identified.

The criterion for acceptable picks of T_0 and $\bar{V}$ from the contoured RMS velocity scans was that the computed interval velocities should agree with ultrasonic measurements within 10 percent. Normally it would be expected that the interval velocities might be lower than the laboratory measurements, since rock units in the field are often fractured and weathered, whereas the samples used for ultrasonic measurements were fresh. This was found to be the case for Honaker velocities computed from T_0 and $\bar{V}$ picks from RMS velocity scans of Bane 1-1, 1-2, 2-1, 2-2, 2-3, and 3-1. Honaker interval velocities ranged from 7.0 to 7.3 km/sec which averaged about 2.5 percent lower than the average ultrasonic velocity. Computed thicknesses varied from 22 meters at the east end of the spread to 98 meters at the west end, although the variation was not monotonic.

Computed interval velocities for the Rome were higher than the laboratory measurements in all cases. This can be explained by the

fact that the Rome shale exposed at Bane contains interbedded layers of high-velocity Rome dolomite. This is sufficient to raise the average velocity of the Rome, the layers of dolomite not being thick enough to give unique reflections and correlation patterns. Computed interval velocities for the Rome varied between 3.7 and 4.5 km/sec. The computed thickness of the Rome at the east end of the spread was 102 meters, but at the west end the thickness was 179 meters, which varies significantly from Cooper's (1964) estimate of 105 meters and Whitman's (1964) estimate of 120 meters.

Below the base of the Rome, normal moveout is insufficient for a velocity analysis to yield unique values of the RMS velocity. T_0-times of events can still be picked, however, which is useful for detecting reflections. The lack of reliable picks of velocity means that little can be said about the thicknesses of these units or the depths to reflectors.

On six RMS velocity scans and on four velocity-filtered records an event between 0.6 and 0.8 second was detected. On every RMS scan and on four velocity-filtered records there is an event between 1.0 and 1.1 seconds. This is the most persistent event to be found on any of the records and remains regardless of the type of frequency filtering or variation in deconvolution parameters. A typical velocity scan including this event is shown in Figure 18a. Figure 18b shows the seismic data from which the velocity analysis was derived. It is noteworthy that the seismic event cannot be identified by visual examination of the seismogram, and is

48

RMS VELOCITY, KM/SEC

T_o — TIME, SEC

SECONDS
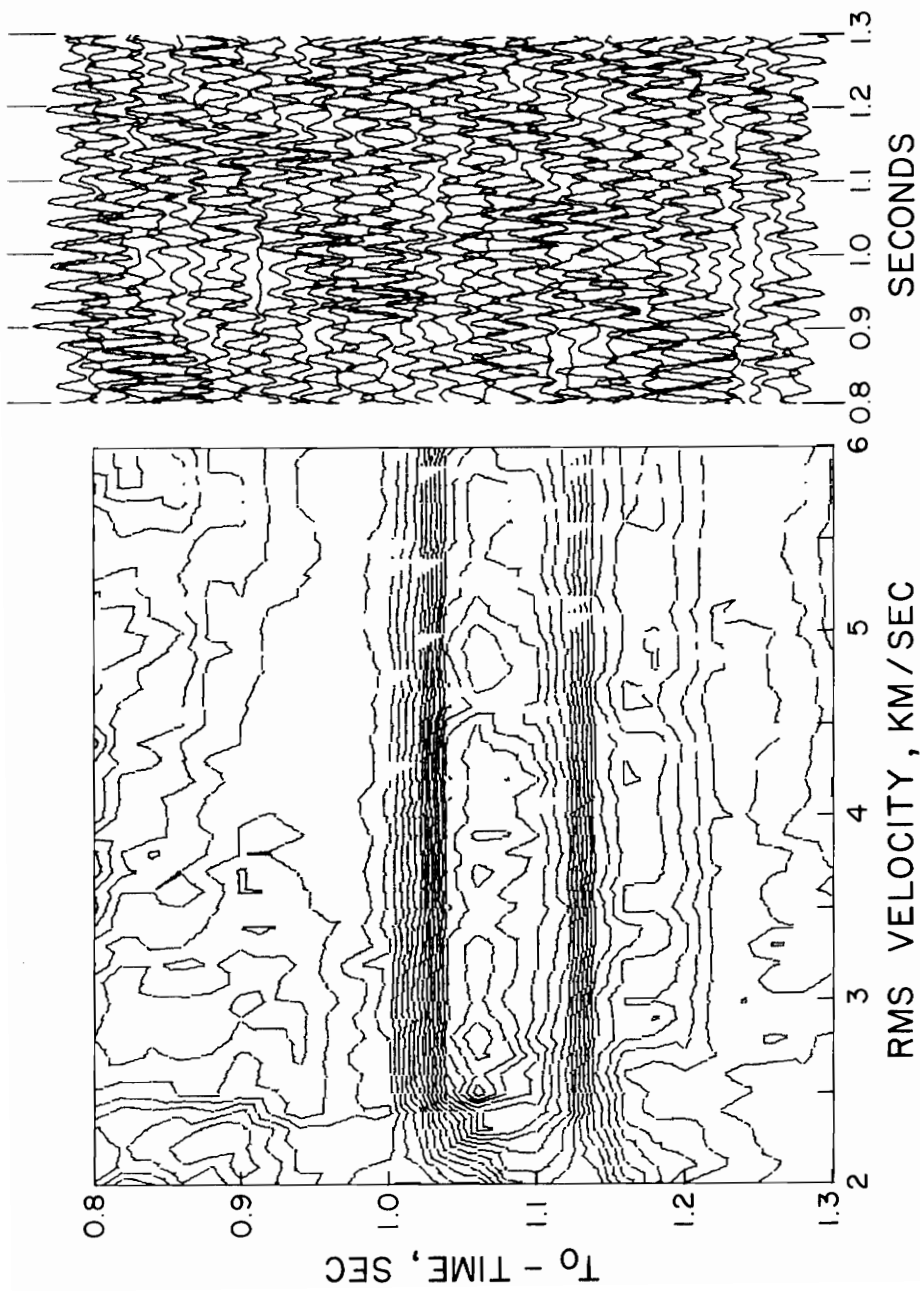
a. Velocity analysis

b. Seismogram

Figure 18. Bane I-I. Filter: 28-54 Hz.

confirmed only after velocity analysis. The impossibility of determining an RMS velocity for this event means that nothing definite can be said about the depth to the reflector. A conservative estimate of 5.5 km/sec for an RMS velocity, ignoring any intervening units between the Rome and this event, and choosing an average T_O-time of 1.05 seconds gives an interval velocity of 5.6 km/sec, a thickness of 2.7 km, and a depth of 2.85 km. This depth agrees well with the depth-to-basement estimate of two to three kilometers published by Sears and Robinson (1971) for the Bane anticline. It is possible, therefore, that a thick, but not necessarily repeated, sedimentary section overlies the Precambrian basement at Bane.

There are, however, valid arguments against such a conclusion. If a Cambrian section with the Unicoi at the base is assumed, there may not be a contrast in acoustic impedance high enough to result in a reflection coefficient of sufficient magnitude to produce the event of remarkable persistency which has been observed. While Table 6 is probably not inclusive of all rock types beneath the Bane Dome, there is no way to justify the large reflection coefficient that is suggested by the persistent event at about one second if an unbroken sedimentary section is assumed. A reflection coefficient of 0.2 would be regarded as large. Values of 0.1 are found in abundance in sedimentary sections, and lower values in profusion (O'Doherty and Anstey, 1971). The reflection coefficient computed from the data in Table 6 for the Rome-Shady

interface ranges from 0.29 to 0.33. Reflection coefficients computed for assumed basement and near-basement rocks in Table 6 are considerably lower, and vary from 0.11 to 0.15. The presence of a thrust fault breccia zone might have associated with it a large reflection coefficient. Also, there is a persistent event at about 2.8 seconds common to nine velocity scans, and this is a further argument for possible repetition of sedimentary units at greater depth. A graphical summary of T_0 picks from the RMS velocity analyses is given in Figure 19, which represents the time duration of correlation patterns as observed on the analyses. The shot-points are arranged in order geographically from west to east.

Whether the event between 1.0 and 1.1 seconds represents a reflection from the basement, a fault zone bringing into contact units with differing acoustic impedances, or a low-velocity breccia zone cannot be determined from the seismic data of this study. Evidence of deeper reflections and the presence of a large reflection coefficient favor the interpretation of a thrust fault and "thin-skinned" tectonics, perhaps as proposed by Milici (1970, Figure 6). The most that can be said for the event between 1.0 and 1.1 seconds is that it represents a good contrast in acoustic impedance.
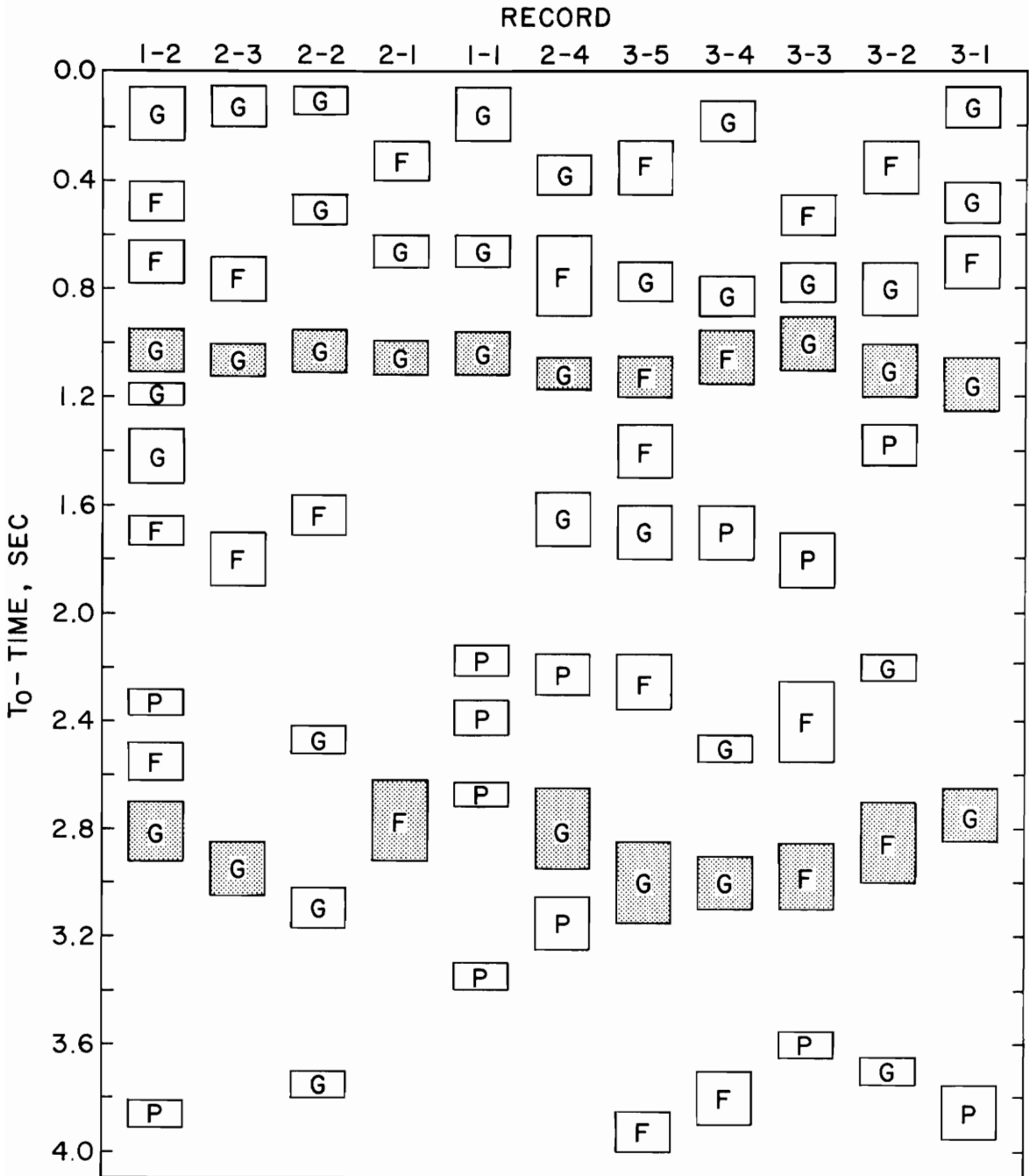
Figure 19.   Summary of RMS velocity analyses showing duration
of correlation patterns.   G = well-defined pattern ,
F = fair ,   P = poor .

REFERENCES

Bogert, B. P., 1962, Correction of seismograms for the transfer
    function of the seismometer: Bull. Seism. Soc. Amer.,
    v. 52, p. 781 - 792.

Cooley, J. W., and Tukey, J. W., 1965, An algorithm for the machine
    calculation of complex Fourier series: Mathematics of
    Computation, v. 19, p. 297 - 301.

Cooper, B. N., 1961, Grand Appalachian field excursion: Va. Poly.
    Inst. and State Univ. Dept. of Geol. Sci. Guidebook no. 1,
    Blacksburg, 187 p.

_____, 1964, Relation of stratigraphy to structure in the
    southern Appalachians, in Tectonics of the Southern
    Appalachians: edited by W. D. Lowry, Va. Poly. Inst. and
    State Univ. Dept. of Geol. Sci. Mem. no. 1, Blacksburg,
    p. 81 - 114.

_____, 1968, Profile of the folded Appalachians of western
    Virginia: Univ. Missouri (Rolla) J., no. 1, p. 27 - 64.

_____, 1971, Appalachian structural and topographic front between
    Narrows and Beckley, Virginia and West Virginia, in Guidebook
    to Appalachian Tectonics and Sulfide Mineralization of
    Southwestern Virginia: Va. Poly. Inst. and State Univ. Dept.
    of Geol. Sci. Guidebook no. 5, Blacksburg, p. 87 - 142.

Costain, J. K., and Robinson, E. S., 1972, Some seismic measurements
    on the Virginia coastal plain: Va. Poly. Inst. and State Univ.
    Water Resources Research Center Bull., no. 56, Blacksburg,
    69 p.

Currier, L. W., 1935, Zinc and lead region of southwestern
     Virginia: Va. Geol. Surv. Bull., no. 43, 122 p.

Dix, C. H., 1955, Seismic velocities from surface measurements:
     Geophysics, v. 20, p. 68 - 86.

Embree, P., Burg, J. P., and Backus, M. M., 1963, Wide band
     velocity filtering — the pie slice process: Geophysics,
     v. 28, p. 948 - 974.

Fail, J. P., and Grau, G., 1963, Les filtres en éventail:
     Geophysical Prospecting, v. 11, p. 131 - 163.

Gwinn, V. E., 1964, Thin-skinned tectonics in the Plateau and
     northwestern Valley and Ridge provinces of the central
     Appalachians: Bull. Geol. Soc. Amer., v. 75, p. 863 - 900.

King, P. B., 1950, Tectonic framework of southeastern United
     States: Bull. Amer. Assoc. Pet. Geol., v. 34, p. 635 - 671.

_____, 1964, Further thoughts on tectonic framework of south-
     eastern United States, in Tectonics of the Southern
     Appalachians: edited by W. D. Lowry, Va. Poly. Inst. and State
     Univ. Dept. of Geol. Sci. Mem. no. 1, Blacksburg, p. 5 - 31.

Lowry, W. D., 1957, Implications of gentle Ordovician folding in
     western Virginia: Bull. Amer. Assoc. Pet. Geol., v. 41,
     p. 643 - 655.

Milici, R. C., 1970, The Allegheny structural front in Tennessee
     and its regional tectonic implications: Amer. J. Sci.,
     v. 268, p. 127 - 141.

Miller, R. L., 1944, Geology and manganese deposits of the Glade
    Mountain district, Virginia: Va. Geol. Surv. Bull.,
    v. 61, 150 p.

_____, 1945, Relation of overthrust faults in southwest Virginia
    (abs.): Bull. Geol. Soc. Amer., v. 56, p. 1182 - 1183.

O'Doherty, R. F., and Anstey, N. A., 1971, Reflections on
    amplitudes: Geophysical Prospecting, v. 19, p. 430 - 458.

Peacock, K. L., and Treitel, S., 1969, Predictive deconvolution:
    theory and practice: Geophysics, v. 34, p. 155 - 169.

Robinson, E. A., 1967, Multichannel time series analysis with
    digital computer programs: San Francisco, Holden-Day.

_____, and Treitel, S., 1967, Principles of digital Wiener
    filtering: Geophysical Prospecting, v. 15, p. 311 - 333.

Rodgers, J., 1949, Evolution of thought on the structure of middle
    and southern Appalachians: Bull. Amer. Assoc. Pet. Geol.,
    v. 33, p. 1643 - 1654.

_____, 1953, The folds and faults of the Appalachian Valley and
    Ridge province, in Southeastern Mineral Symposium: Kentucky
    Geol. Surv. Spec. Pub. no. 1, Section 9, p. 150 - 166.

_____, 1964, Basement and no-basement hypotheses in the Jura and
    the Appalachian Valley and Ridge, in Tectonics of the Southern
    Appalachians: edited by W. D. Lowry, Va. Poly. Inst. and State
    Univ. Dept. of Geol. Sci. Mem. no. 1, Blacksburg, p. 71 - 80.

Sears, C. E., and Robinson, E. S., 1971, Relations of Bouguer
    gravity anomalies to geological structure in the New River
    district of Virginia: Bull. Geol. Soc. Amer., v. 82,
    p. 2631 - 2638.

Taner, M. T., and Koehler, F., 1969, Velocity spectra — digital
    computer derivation and applications of velocity functions:
    Geophysics, v. 34, p. 859 - 881.

Whitman, H. M., 1964, Geology of the Pearis Mountain area,
    Virginia: M.S. thesis, Dept. of Geol. Sci., Va. Poly.
    Inst. and State Univ., Blacksburg.

Appendix I. Digital frequency filtering

A cosine-tapered frequency passband was used for the digital filtering. Bogert (1962) gives the following equations for such a filter:

$$T(f) = \begin{cases} 0 & \text{for } f \leq f_0 \\[2ex] \dfrac{1}{2^k}\left[1 - \cos \pi \dfrac{f - f_0}{f_1 - f_0}\right]^k & \text{for } f_0 \leq f \leq f_1 \\[2ex] 1 & \text{for } f_1 \leq f \leq f_2 \\[2ex] \dfrac{1}{2^\ell}\left[1 - \cos \pi \dfrac{f_3 - f}{f_3 - f_2}\right]^\ell & \text{for } f_2 \leq f \leq f_3 \\[2ex] 0 & \text{for } f_3 \leq f \end{cases}$$

where f is frequency in Hertz, $T(f)$ is the filter amplitude, and k and ℓ are exponents which were set equal to unity in this study. An illustration of the shape of the filter and the definitions of f_0, f_1, f_2, and f_3 are shown in Figure I-1. The filter passes without distortion frequency components between f_1 and f_2 while eliminating those below f_0 and above f_3.
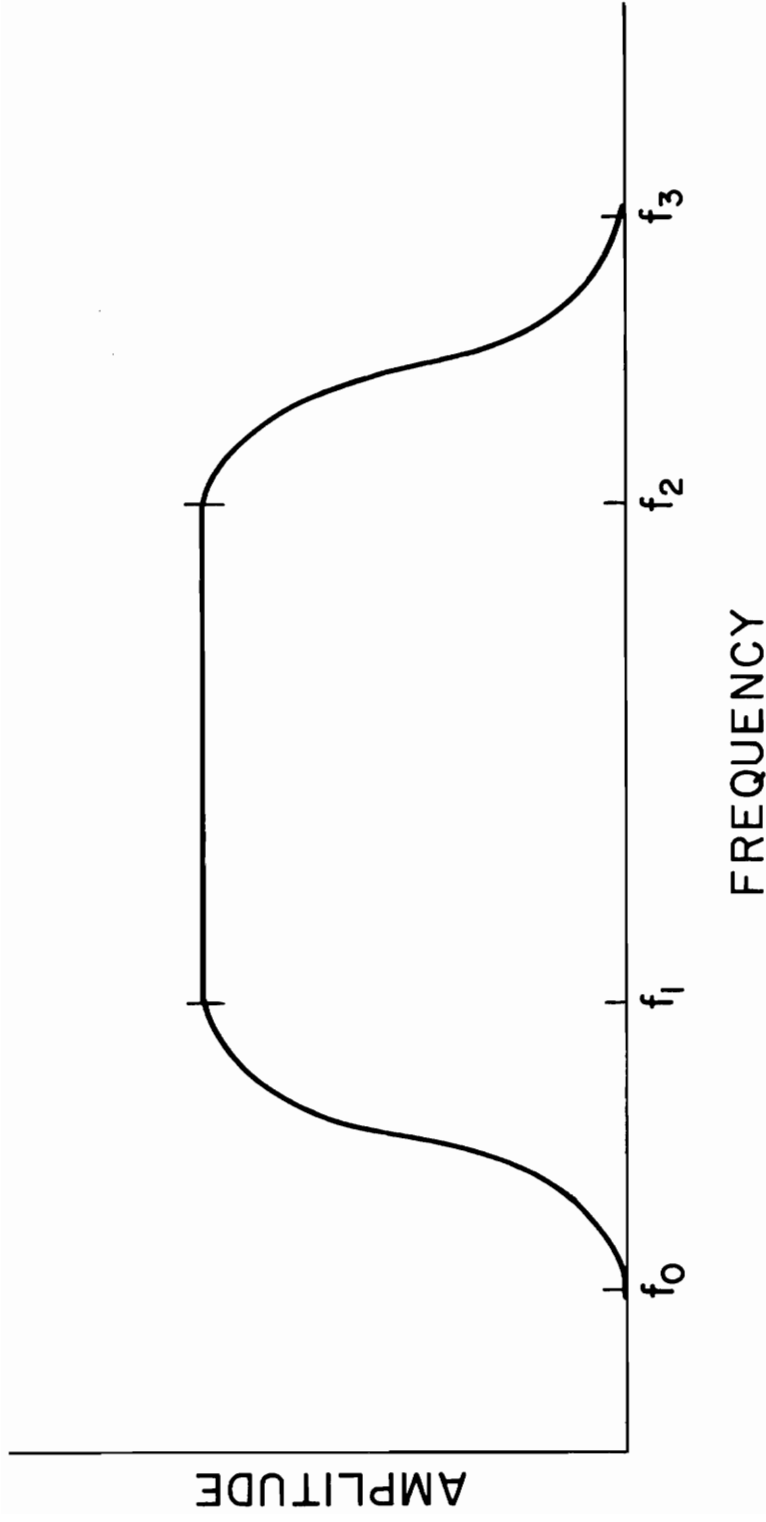
Figure I-I. Cosine – tapered passband filter
(After Bogert, 1962)

Appendix II. RMS velocity analysis

A simple but typical geophone array is shown in Figure II-1, where the surface and reflector are flat and parallel. Consider ray path SRG in Figure II-1. Let T_0 be the two-way traveltime of a signal starting from the source S to a point directly below the source on the reflector and back to the surface. The two-way traveltime along the slant path SRG is denoted by T. The source of the reflected signal can be considered to be at S', the image position of S, located a distance 2z below S. The relationship between T and T_0 can then be given by:

$$T = (T_0^2 + \frac{x^2}{V^2})^{\frac{1}{2}} \qquad (II-1)$$

where x is the horizontal shotpoint – geophone distance SG. This is the equation of a hyperbola.

Figure II-2 is essentially the same as Figure II-1, except that a reflection is shown superposed on the hyperbolic traveltime curve as the reflected signal arrives at each geophone. By rearranging equation II-1 an expression for the velocity V can be obtained:

$$V = \left[\frac{x^2}{T^2 - T_0^2} \right]^{\frac{1}{2}} \qquad (II-2)$$

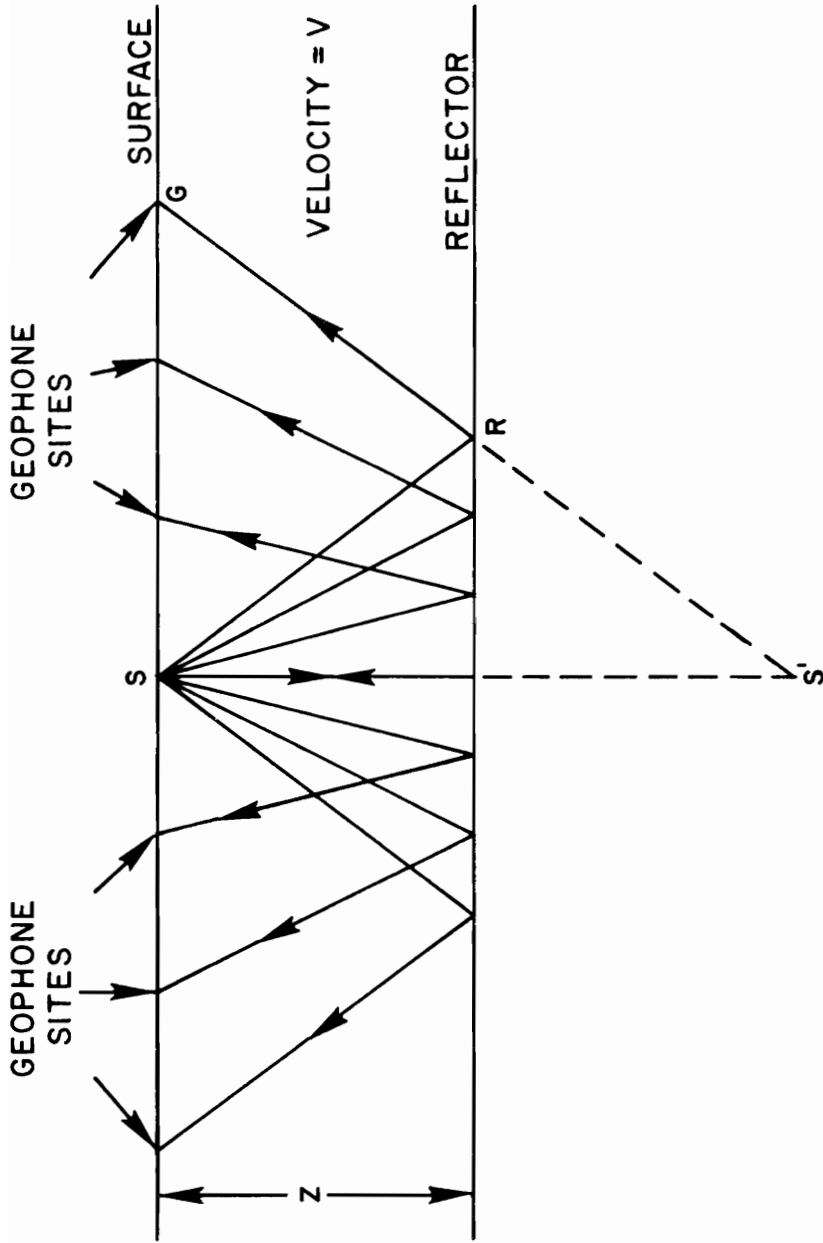The problem with applying this relationship directly to find veloc-

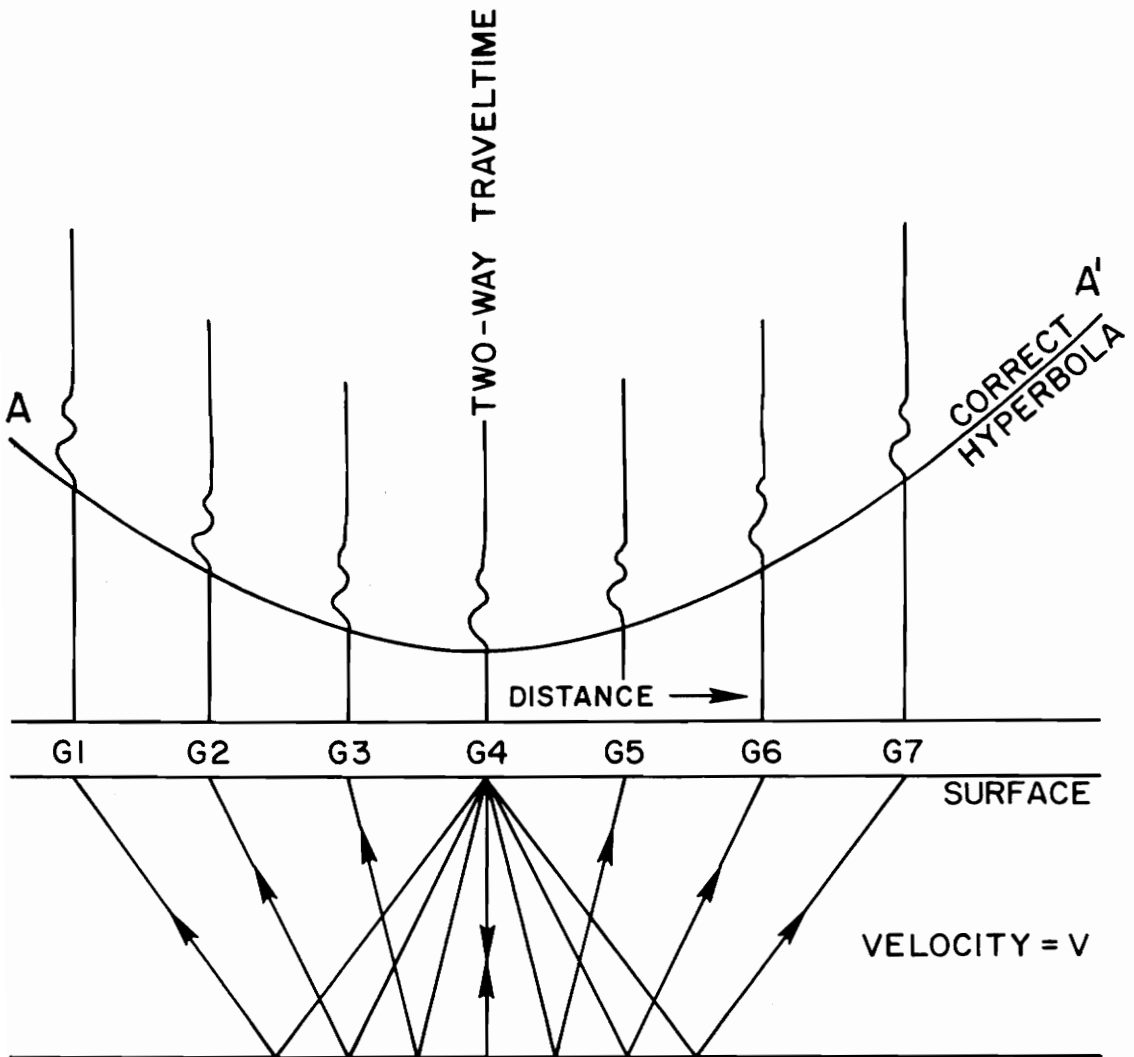Figure II-1. Idealized raypaths from a shot-point to a geophone spread.

Figure II-2. Reflection from a single interface showing hyperbolic traveltime.

ity is that it is usually difficult to determine where a reflection begins on a seismogram, making the determination of T_0 and T inaccurate.

Figure II-3 shows each seismic trace with the single reflection aligned within a "window" which coincides with the hyperbolic traveltime curve AA'. It is apparent that if the waveforms within each window are, for example, summed, then since all of the reflections are in the same position with respect to the window, the peaks and troughs will reinforce each other, and constructive interference will add peaks to peaks and troughs to troughs. The waveform resulting from the sum of the individual reflections will be much larger than any single reflection. On the other hand, if the window tracks a different hyperbola BB', it is apparent that when the points within each window are summed, the reflections are not in phase with each other, and some destructive interference will take place. But the hyperbola AA' is a consequence of using the correct velocity, V; the hyperbola BB' is associated with some other, incorrect, velocity, V'. Evidently, if the windows are placed on the traces so that they track a hyperbola that is associated with the correct velocity, V, then a high degree of correlation between traces will result. If the windows are placed so that they follow a hyperbola that is associated with a velocity other than the correct one, a lower degree of correlation will result. If the correct velocity is unknown, then a number of velocities can be tested. Each velocity will correspond to a unique hyperbola.
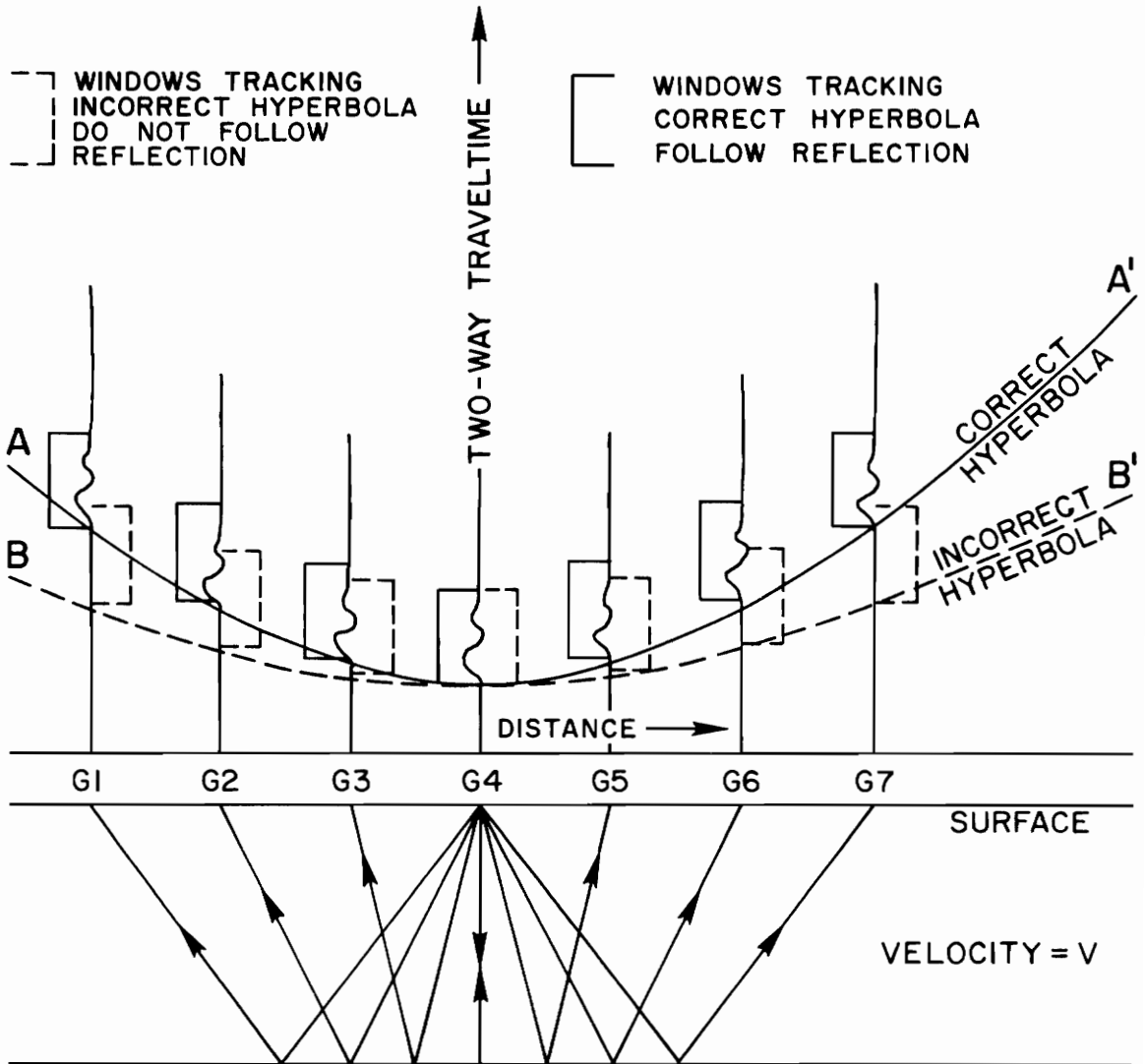
Figure II-3. Relationship between correct and incorrect scanning hyperbolas.

Each hyperbola will give a measure of the coherence, or correlation, between traces. The highest correlation is associated with that hyperbola corresponding to the correct velocity, V. The search for the correct velocity is called a hyperbolic scan. Scans are made beginning with some velocity value assumed to be lower than the correct value and ending with a velocity assumed to be higher than the correct value.

One quantitative measure of correlation between the contents of the windows of each trace is the semblance coefficient, described by Taner and Koehler (1969):

$$S = \frac{\sum\limits_{j=k-(N/2)}^{k+(N/2)} \left[\sum\limits_{i=1}^{M} a_{i,j(i)}^2 \right]^2}{M \sum\limits_{j=k-(N/2)}^{k+(N/2)} \left[\sum\limits_{i=1}^{M} a_{i,j(i)}^2 \right]} \qquad (II-3)$$

where M is the number of traces, i is the trace number, N+1 is the number of points in the window, and $a_{i,j(i)}$ is the amplitude of the jth point on the ith trace. This coefficient varies between 0 and 1. The velocity associated with the highest value of semblance indicates the correct hyperbolic scan, and therefore, the correct velocity, V.

If more than one reflector is present, it is no longer possi-

ble to express the traveltime, T, as a function of the distance to the geophone, x, with a single equation. The traveltime curve is no longer a simple hyperbola, and the velocity to the deeper reflector becomes the root mean square (RMS) velocity given by Dix (1955):

$$\overline{V}_m^2 = \frac{\displaystyle\sum_{i=1}^{M} (V_i^2 \, \Delta t_i)}{T_0} \qquad \text{(II-4)}$$

where $\overline{V}_m$ is the RMS velocity down to the base of the mth layer, V_i is the interval velocity of some intermediate i^{th} layer, Δt_i is the two-way time spent traversing the ith layer, and T_0 is the vertical two-way traveltime to the base of the mth layer. The velocity, $\overline{V}$, the square root of the mean of the squares of the interval velocities, replaces V in equation (II-1):

$$T = (T_0^2 + \frac{x^2}{\overline{V}^2})^{\frac{1}{2}} \qquad \text{(II-5)}$$

and hyperbolic scans, which are based on this equation, now scan the seismogram for an RMS velocity instead of an interval velocity. The true interval velocities can be recovered from the RMS velocities by use of the relation (Dix, 1955):

$$V_m = \left[\frac{\bar{V}_m^2 T_{O_m} - \sum_{i=1}^{M} V_i^2 \, \Delta t_i}{\Delta t_m} \right]^{\frac{1}{2}} \qquad \text{(II-6)}$$

If there are two layers, there are two RMS velocities. The interval velocity and the RMS velocity corresponding to the first layer are identical. The interval velocity of the second layer must then be computed from the RMS velocity associated with the reflection from the bottom of the second layer.

When there is more than one reflection on the seismogram, a reflection velocity analysis becomes a two-dimensional search for 1) reflections arriving at different T_O-times, and 2) the correct RMS velocity associated with the reflection arriving at a particular T_O-time. Semblance coefficients are computed for all combinations of T_O and $\bar{V}$, where T_O might range from, say, 0.0 to 2.0 sec, and $\bar{V}$ from 2 to 6 km/sec. This matrix of semblance coefficients is then contoured. High values of semblance at a particular value of T_O and $\bar{V}$ mean that a reflection (primary, multiple, or other coherent event) has arrived at time T_O with the corresponding value of $\bar{V}$. If the reflections are well-separated in time, it is often possible to pick several pairs of values of T_O and $\bar{V}$ and compute interval velocities for comparison with interval velocities determined by other methods, for example by refraction techniques. If the reflections are not well-separated in time, the determination of interval velocities from a single record becomes difficult,

if not impossible, due to overlap of the individual reflections.

(NOTE: The preceding four paragraphs were either taken verbatim or adapted from Costain and Robinson, 1972, pages 10 - 12.)

Appendix III. Predictive deconvolution

The advent of the digital computer has led to new approaches to the processing and interpretation of seismic data. Digital filters can now be designed for practically any purpose. A basic model for the filtering process consists of an input signal, a desired output signal, and an actual output signal. By minimizing the difference between the actual and desired outputs in a least-squares sense, it is possible to obtain the "optimum linear filter," also known as the Wiener filter, named for Norbert Wiener, the chief originator of the theory of statistical communication (Robinson and Treitel, 1967).

A brief illustration of the mathematics involved in the derivation of the optimum linear filter follows. Consider a minimum delay wavelet of the form:

$$b = (b_0, b_1, b_2, \ldots, b_n)$$

A minimum delay wavelet is used because deconvolution, a type of inverse filtering, requires a minimum delay wavelet.

The desired output is $d_t = (d_0, d_1, d_2, \ldots, d_k)$

The filter is $f_t = (f_0, f_1, f_2, \ldots, f_m)$

The actual output, obtained by the convolution $b_t * f_t$, is

$$c_t = (c_0, c_1, c_2, \ldots, c_{m+n})$$

In order to make c_t as much like d_t as possible in a least-squares sense, it is necessary to determine the filter coefficients f_t such that

$$E = \sum_t (d_t - c_t)^2$$

is a minimum, where E is an error indicator defined as the sum of the squares of the differences between corresponding coefficients of the desired and actual outputs.

$$\text{But } c_t = \sum_{s=0}^{m} f_s b_{t-s} \qquad \text{for } t = 0, 1, 2, \ldots, m+n$$

and $c_t = 0$ for $t \geq m+n+1$

$$\text{Then } E = \sum_{t=0}^{m+n} (d_t - \sum_{s=0}^{m} f_s b_{t-s})^2$$

E will be a minimum if every partial derivative with respect to each coefficient f_0, f_1, f_2, . . . , f_m equals zero; that is, if

$$\frac{\partial E}{\partial f_j} = 0 = 2 \sum_{t=0}^{m+n} (d_t - \sum_{s=0}^{m} f_s b_{t-s})(-b_{t-j}) \qquad \text{for } j=0,1,2,\ldots,m$$

Expanding the above expression and rearranging terms gives:

$$f_s \left[\sum_{s=0}^{m} b_{t-s} b_{t-j} \right] = \sum_{t=0}^{m+n} d_t b_{t-j} \qquad \text{for } j = 0, 1, 2, \ldots, m$$

Let $b_t = b_0, b_1$

Then, for $s = (0,1)$ and $j = 0$,

$$f_0(b_0 b_0 + b_1 b_1) + f_1(b_0 b_1) = d_0 b_0 + d_1 b_1$$

But $b_0 b_0$ and $b_1 b_1$ are the autocorrelation of b_t in the zero-shift position, and $b_0 b_1$ is the autocorrelation in the first unit-shift position. $d_0 b_0$ and $d_1 b_1$ are the crosscorrelation of d_t and b_t in the zero-shift position. Letting r_t represent the autocorrelation and g_t the crosscorrelation gives:

$$f_0 r_0 + f_1 r_1 = g_0$$

Letting $s = (0,1)$ and $j = 1$ gives:

$$f_0 r_1 + f_1 r_0 = g_1$$

These equations in matrix form are:

$$\begin{bmatrix} r_0 & r_1 \\ r_1 & r_0 \end{bmatrix} \begin{bmatrix} f_0 \\ f_1 \end{bmatrix} = \begin{bmatrix} g_0 \\ g_1 \end{bmatrix}$$

The square matrix in r is called a Toeplitz matrix. These

equations can be represented in general as

$$\sum_{s=0}^{m} f_s r_{j-s} = g_j \qquad ; \qquad j = 0, 1, 2, \ldots, m$$

This gives a set of m+1 linear algebraic equations (called the "normal equations") in m+1 unknowns. Solving the normal equations for f_t gives the coefficients of the least-squares Wiener linear filter.

Since f_t can be any filter, it can just as well be an inverse spiking filter, but since f_t only exists in positive time, the wavelet on which it operates must be minimum delay. For any general filter, f_t, the output, y_τ, is equal to the input, x_t, convolved with the filter; that is,

$$y_\tau = x_t * f_t$$

or

$$y_\tau = \sum_t x_t f_{\tau - t}$$

If f_t is a prediction filter with a prediction distance α, then the output y_τ will be an estimate of the input x_t at some future time $t+\alpha$. Then

$$y_\tau = \sum_t x_t f_{\tau - t} = \hat{x}_{t+\alpha}$$

where $\hat{x}_{t+\alpha}$ is an estimate of $x_{t+\alpha}$ (Peacock and Treitel, 1969).

An error series e may be defined as the difference between the actual value $x_{t+\alpha}$ and the predicted value $\hat{x}_{t+\alpha}$;

$$e_{t+\alpha} = x_{t+\alpha} - \hat{x}_{t+\alpha} = x_{t+\alpha} - \sum_t x_t f_{\tau-t}$$

In z-transform notation:

$$z^{-\alpha} E(z) = z^{-\alpha} X(z) - X(z)f(z)$$

or $$E(z) = X(z) - z^{\alpha} X(z)F(z) = X(z)(1 - z^{\alpha} F(z))$$

where $(1 - z^{\alpha} F(z))$ is the z-transform of the so-called prediction error operator. In the time domain the prediction error operator, a_t, is

$$a_t = 1, 0, 0, 0, \ldots, 0, -f_0, -f_1, \ldots, -f_m$$

$$\underbrace{}_{\alpha - 1 \text{ zeros}}$$

where the series f_0, f_1, . . . , f_m is determined from the solution of the normal equations discussed above.

Deconvolution, then, is actually a "shaping" or "pulse compression" operation. If $\alpha = 1$, then the deconvolution process becomes a "spiking" operation. Predictive deconvolution works by predicting the future of a seismic trace consisting of a reflected wavelet and its multiples. The predicted future is then subtracted

from the trace beginning after a specified time lag determined by the value of α and generally taken as the second zero-crossing of the autocorrelogram of the trace.

The length of the series f_0, f_1, . . . , f_m should be equal to the length of that part of the autocorrelogram that one desires to cancel out. When working with seismic records consisting of long traces, however, it quite often develops that a short filter length is as effective as a long filter length due to the repetitive nature of the characteristic energy in the trace.

Appendix IV. Velocity filtering

In this multi-channel process, a number of input traces are operated upon simultaneously to produce <u>one</u> output trace. For example, if a particular application of this technique is specified as a 12-channel process, as was the case in all applications in this study, then twelve traces are processed simultaneously to produce one filtered output trace. For the 36-trace seismograms obtained for this study, traces number 1 through 12 are processed first. The first output trace corresponds to trace $6\frac{1}{2}$, or the point on the ground between geophones 6 and 7. Next, traces number 2 through 13 are processed to produce an output trace corresponding to trace $7\frac{1}{2}$. This process is repeated until all 36 traces are used. The result is a "velocity-filtered" record consisting of 25 traces.

It should be noted, however, that this process differs significantly from conventional filtering techniques (for example, frequency filtering) in that each input trace at a different offset is filtered through a different appropriately designed filter response before being summed to form the output trace. Each different filter response is a time-domain operator computed from the expression (Embree and others, 1963):

$$y = \frac{1}{\pi^2\left[\left(\dfrac{x_m}{\Delta x}\right)^2 - n^2\right]} \qquad \text{(IV-1)}$$

where m and n are integers. The formal derivation of this expression is presented in the Appendix to Embree and others (1963). Δx is the interval between recording points in a linear geophone array and is assumed constant between each pair of consecutive points. In this study the spacing between the geophones in the actual spread was not constant, but the deviation was assumed insufficient to adversely affect the application of this filtering technique to the data. X_m is the distance from the mth recording point to the center of the array of geophones whose associated traces are being processed to produce a filtered trace. For example, in an array of twelve geophones, X_1, the distance from recording point #1 to the center of the array, is equal to $(5\frac{1}{2}) \Delta x$. The ratio $X_1/\Delta x$ would then equal simply $5\frac{1}{2}$. The distance X_{12} is the same as X_1, but on the other side of the center. Therefore, $X_{12} = (-5\frac{1}{2}) \Delta x$, and $X_{12}/\Delta x = -5\frac{1}{2}$. By a similar line of reasoning $X_2/\Delta x = 4\frac{1}{2}$ and $X_{11}/\Delta x = -4\frac{1}{2}$, and so on, until finally $X_6/\Delta x = \frac{1}{2}$ and $X_7/\Delta x = -\frac{1}{2}$.

Each operator computed by equation IV-1 is symmetric about the reference point in space and time; that is, it has zero phase shift (Embree and others, 1963). If the number of points in the operator is specified as 21, as was the case in each application in this study, n takes on values from -10 to +10, including zero, in equation IV-1. Since the data are digitized at 2 ms intervals, this operator would extend from -20 to +20 ms.

The effect of this filtering process on a synthetic seismogram consisting of a number of events with different apparent velocities

(Figure IV-1) is shown in Figure IV-2, where the beam direction of the filter is zero ms/trace, and the filter width or passband is 1 ms/trace. Figure IV-3 shows the filter with the same passband, but this time the beam direction has been pointed in the direction of the inclination of the event dipping at 4 ms/trace. Equation IV-1 makes no provision for directing the filter, so the pointing is done by shifting the unfiltered traces of the seismogram until the event dipping at 4 ms/trace lines up vertically. After filtering, the resultant traces are shifted back to their true relative positions in time.

Figure IV-4 is another 36-trace synthetic seismogram that bears a closer resemblance to a real record. This synthetic is based on the shotpoint-geophone distances associated with data record #2. Figure IV-5 is the same synthetic seismogram after velocity filtering with a passband of 2 ms/trace and a beam direction of zero ms/trace. The velocity filter discriminates against the first breaks and early events while leaving relatively unaffected the high velocity events at 1.1 and 1.9 seconds.

An actual seismogram usually does not exhibit such well-behaved events, however, as was evident in Figures 3 and 4 where reflected events, if any, could not be readily identified by visual inspection. Figure IV-6 is the result of velocity filtering record #2 (Figure 3) with no digital frequency filtering. A reflected event is obvious at about 1.05 seconds, and fragments of earlier events are also evident. Figure IV-7 is Figure IV-6 after adding
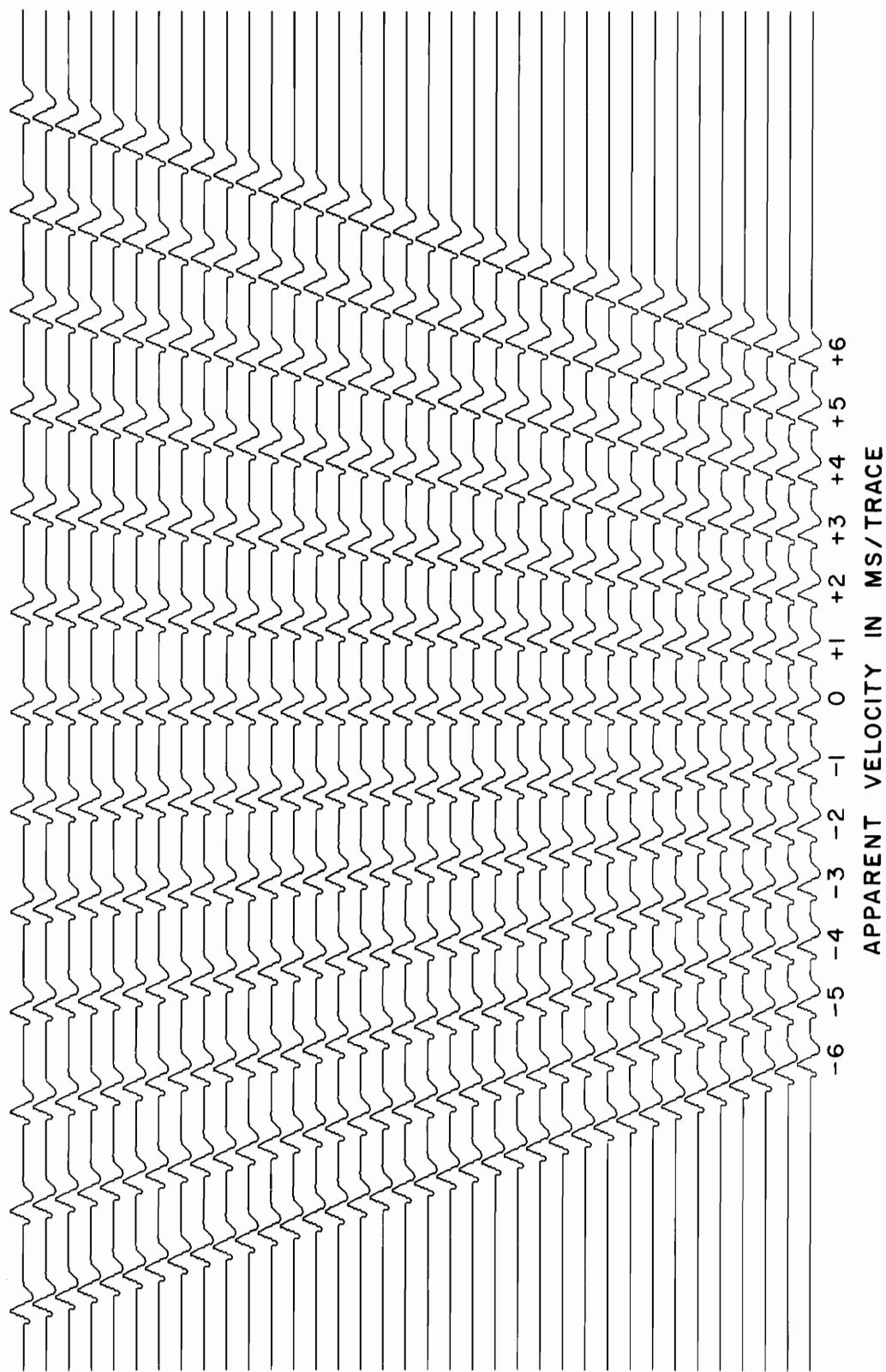
APPARENT VELOCITY IN MS/TRACE

Figure IV-I. Synthetic seismogram for testing velocity filter.

APPARENT VELOCITY IN MS/TRACE

-1   0   +1

Figure IV-2. Result of velocity-filtering Figure IV-1.
Beam direction = 0 ms/trace;
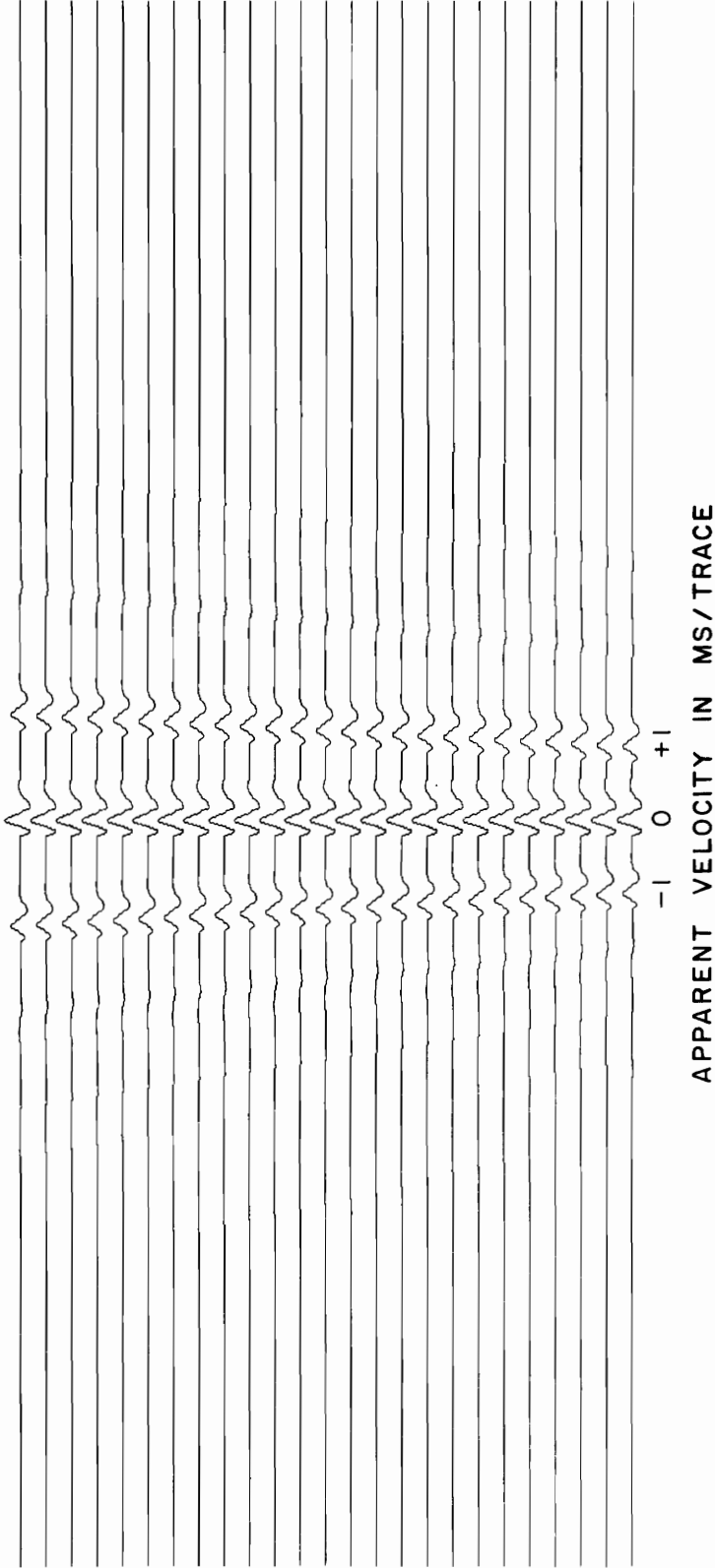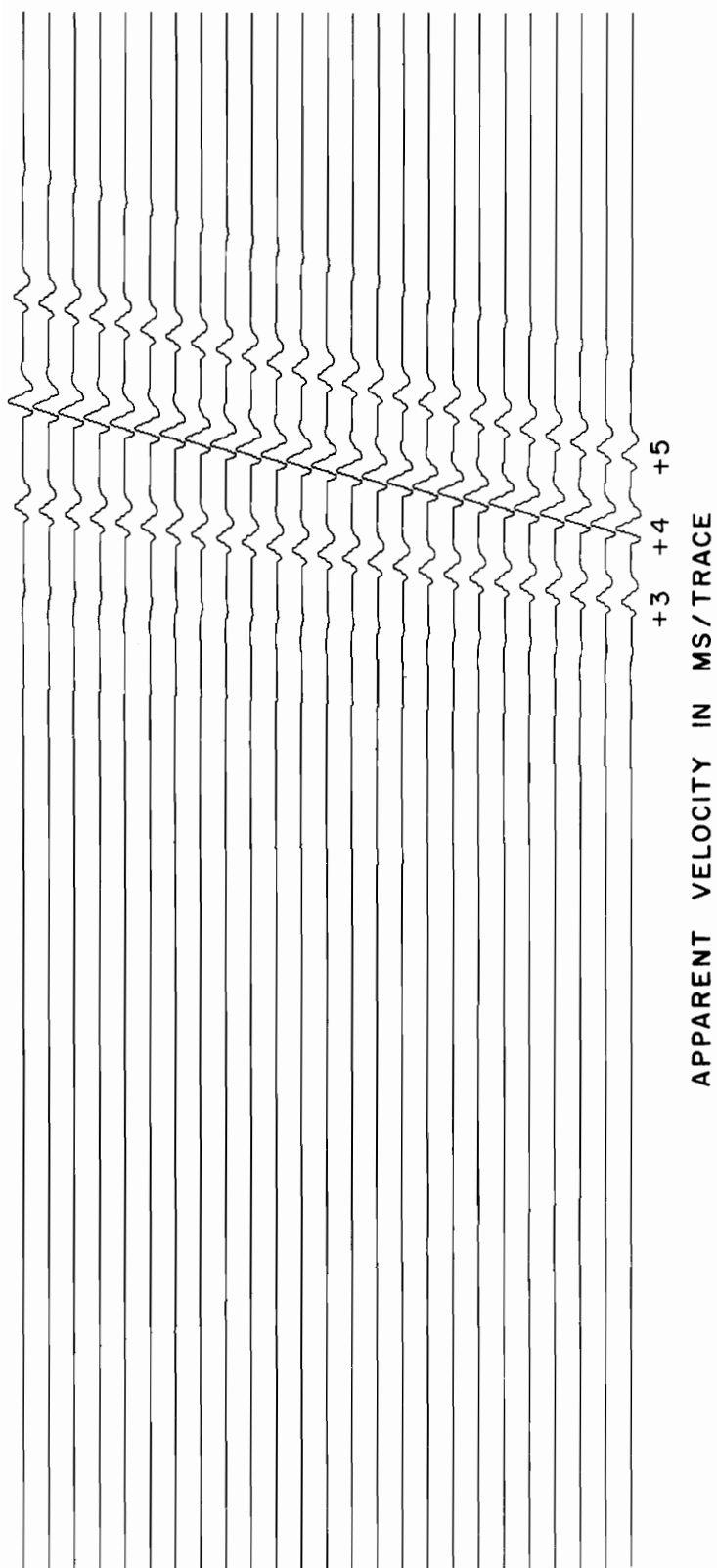passband = ±1 ms/trace.

APPARENT VELOCITY IN MS/TRACE

+3 +4 +5

Figure IV - 3. Result of velocity - filtering Figure IV - I.
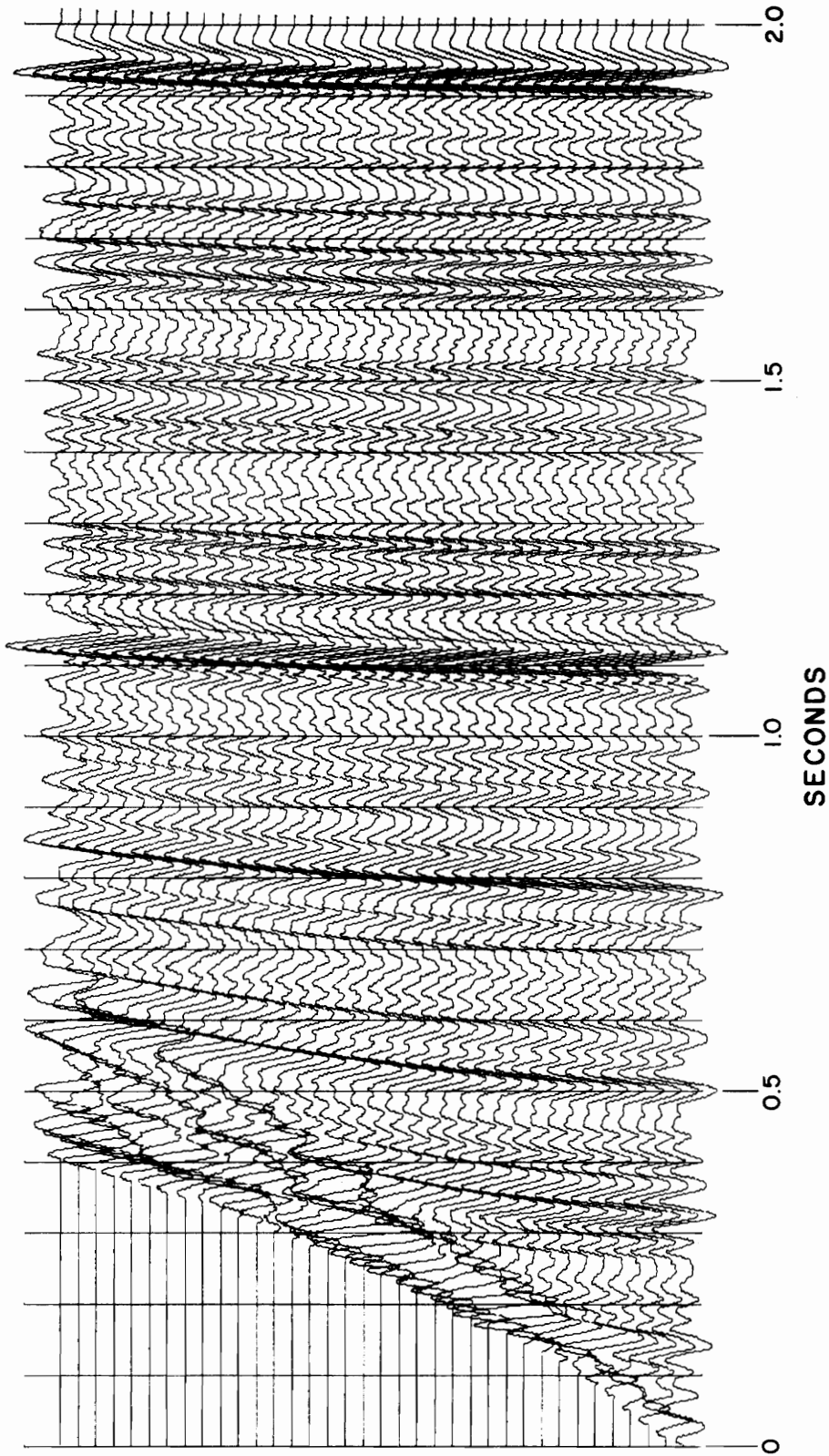Beam direction = +4 ms/trace;
passband = ±I ms/trace.
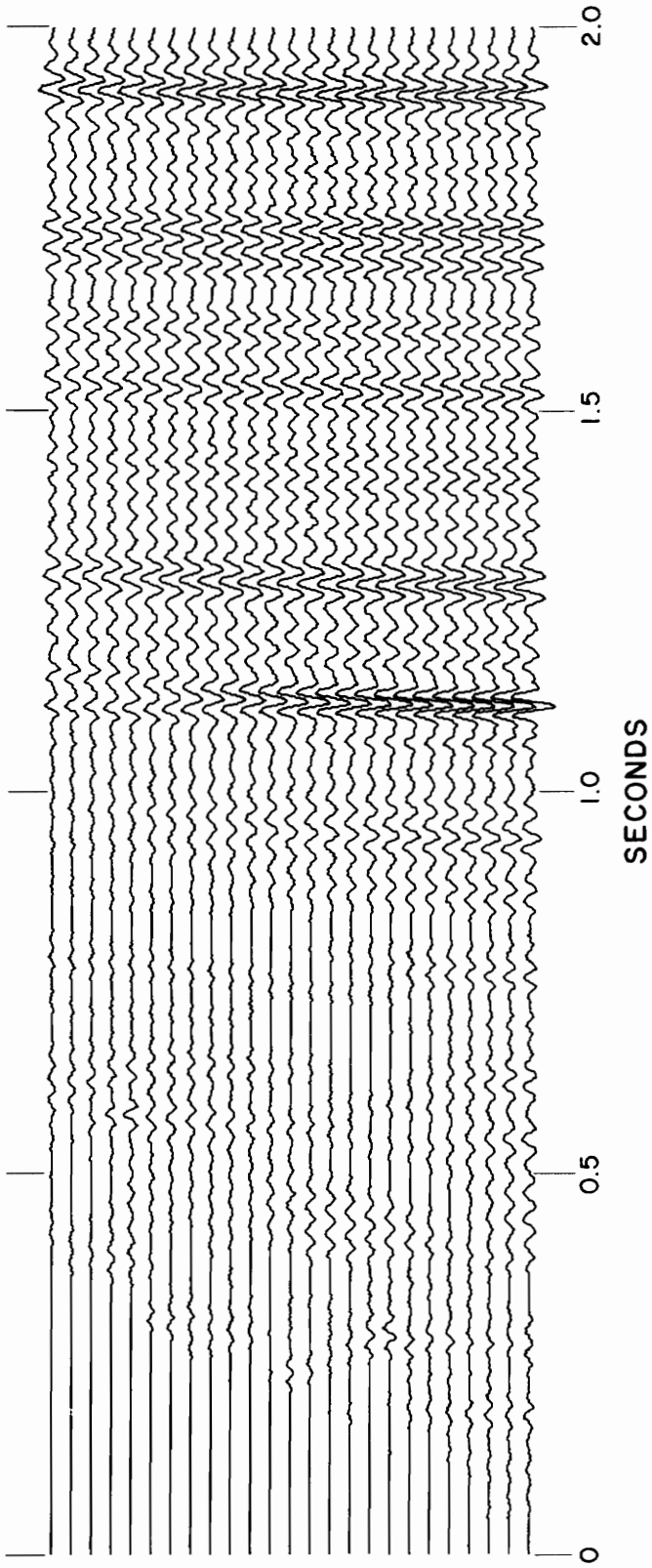
Figure IV - 4. Synthetic seismogram with normal moveout.

Figure IV-5. Result of velocity-filtering Figure IV-4 using a filter passband of ±2 ms/trace and a beam direction of 0 ms/trace.
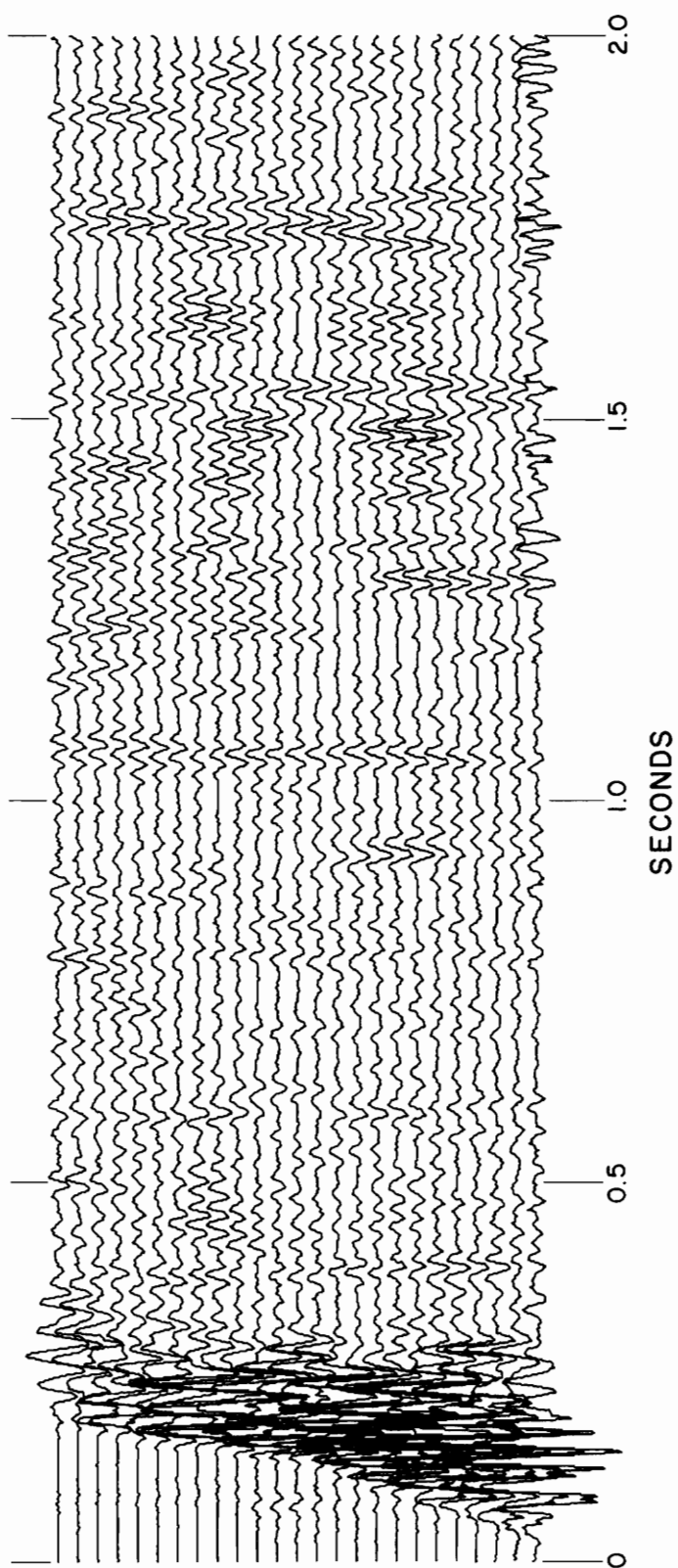
Figure IV – 6. Bane 1–2. Velocity – filtered .
Filter = ± 2 ms / trace ;
beam direction = O ms/trace.
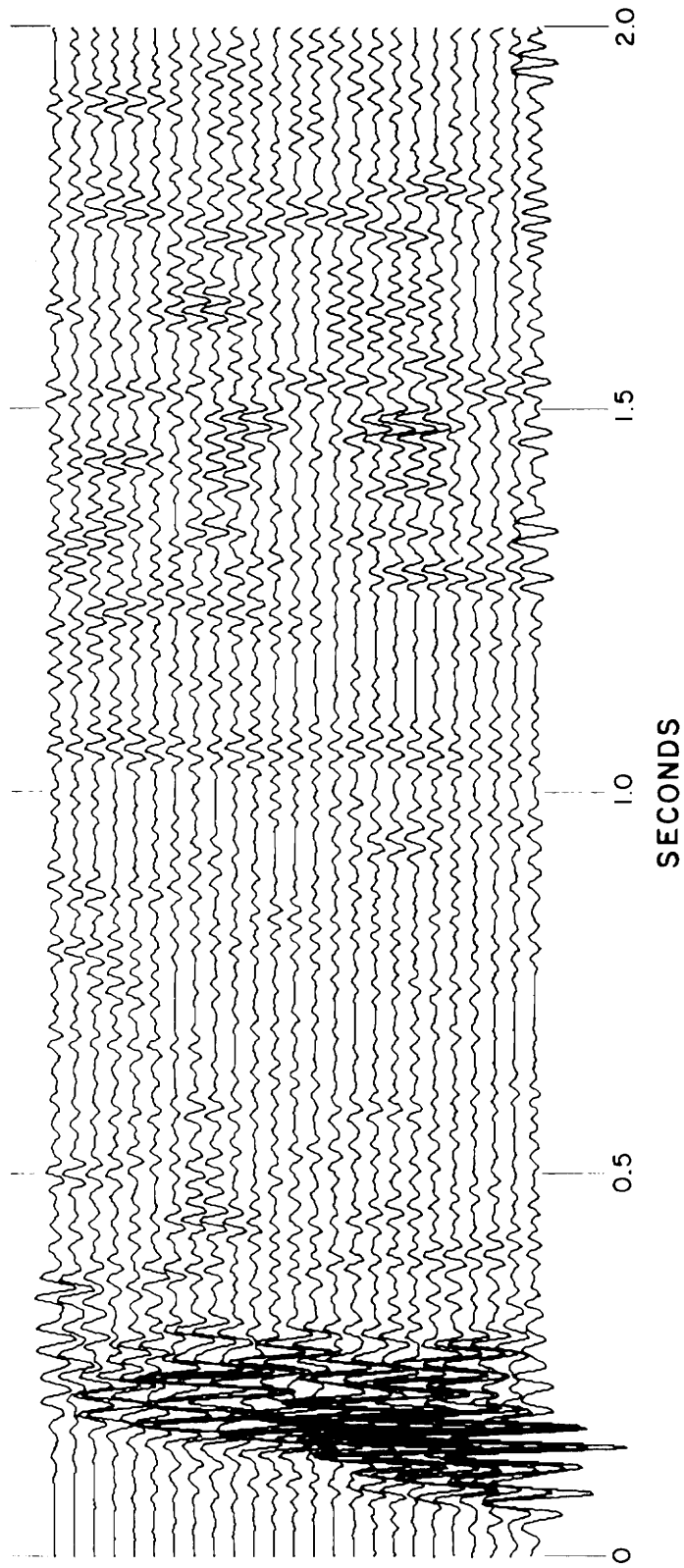
Figure IV-7. Same as Figure IV-6 with frequency filter 28-54 Hz.

a frequency filter. The frequency-filtered data are less satis-
factory, probably because of ringing induced by the cosine-tapered
frequency filter.

Appendix V. Unprocessed seismograms

Figures V-1 through V-11 are the unprocessed records from all eleven shotpoints. These seismograms were electronically filtered in the field during recording; filter parameters and other relevant information are given in Table 1.

85
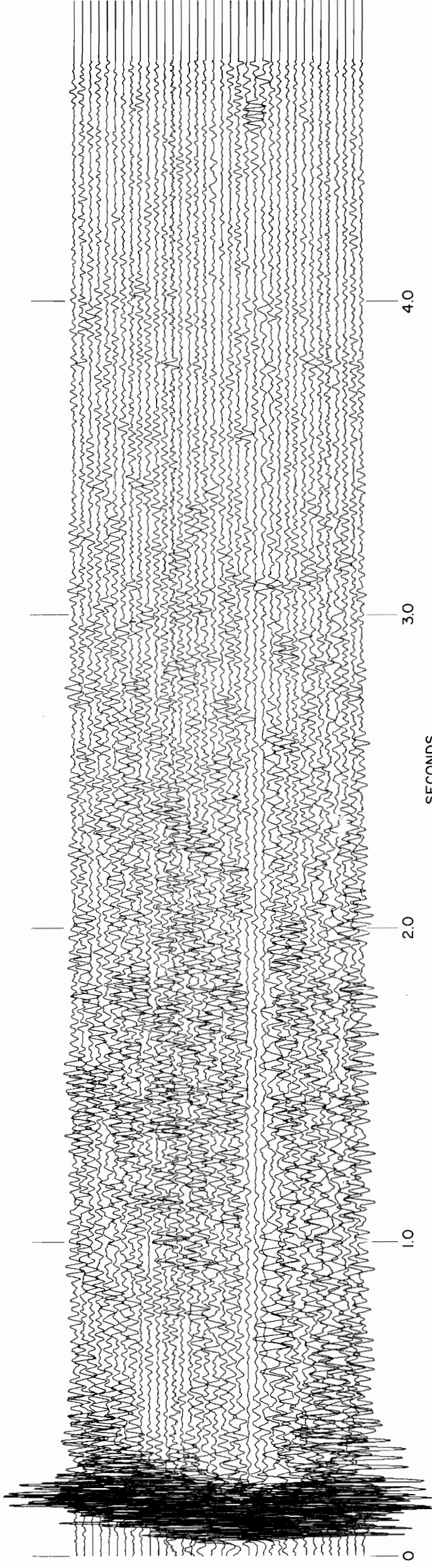
SECONDS
FIGURE V-I
BANE I-I (SHOTPOINT I)
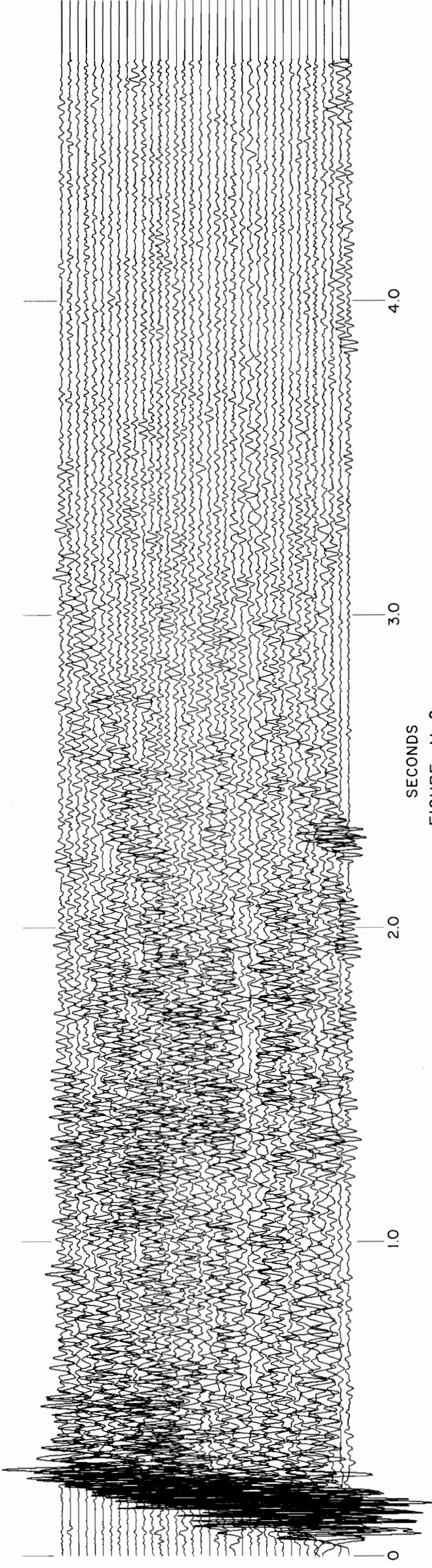
SECONDS
FIGURE V-2
BANE I-2 (SHOTPOINT 2)
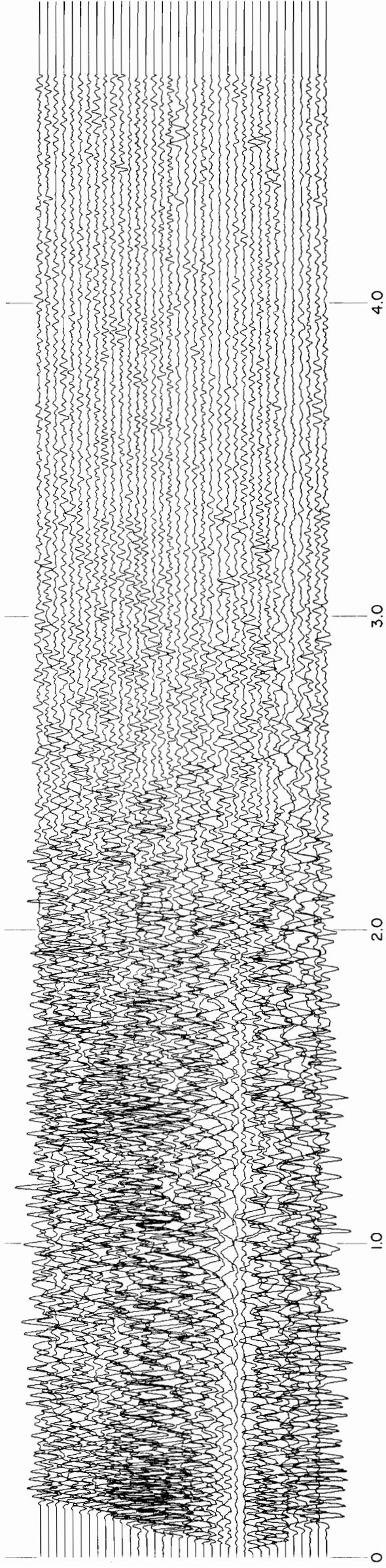
SECONDS
FIGURE V-3
BANE 2-1 (SHOTPOINT 3)
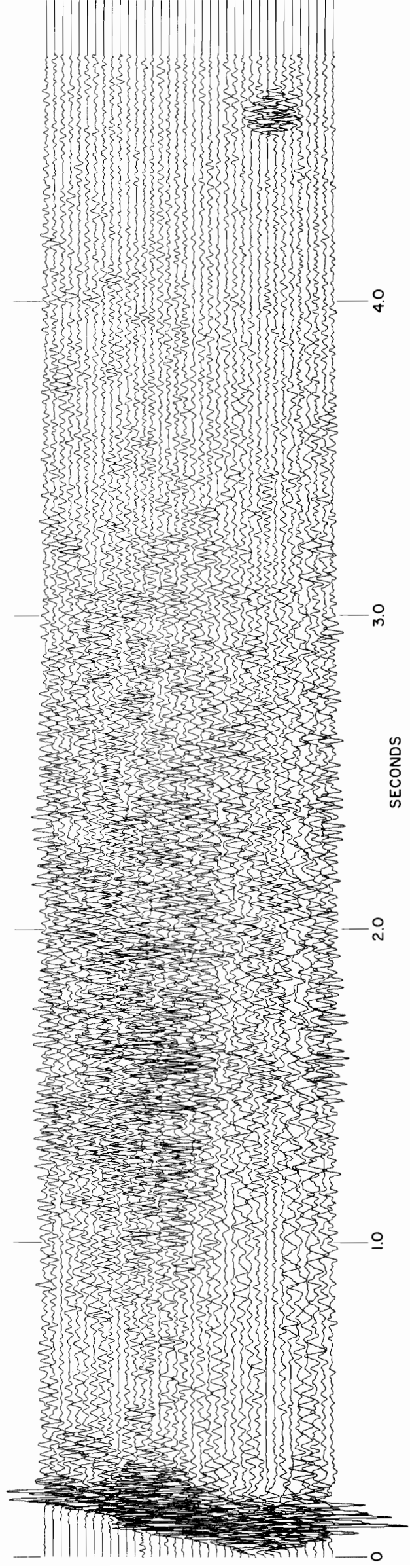
SECONDS
FIGURE V-4
BANE 2-2 (SHOTPOINT 4)

86
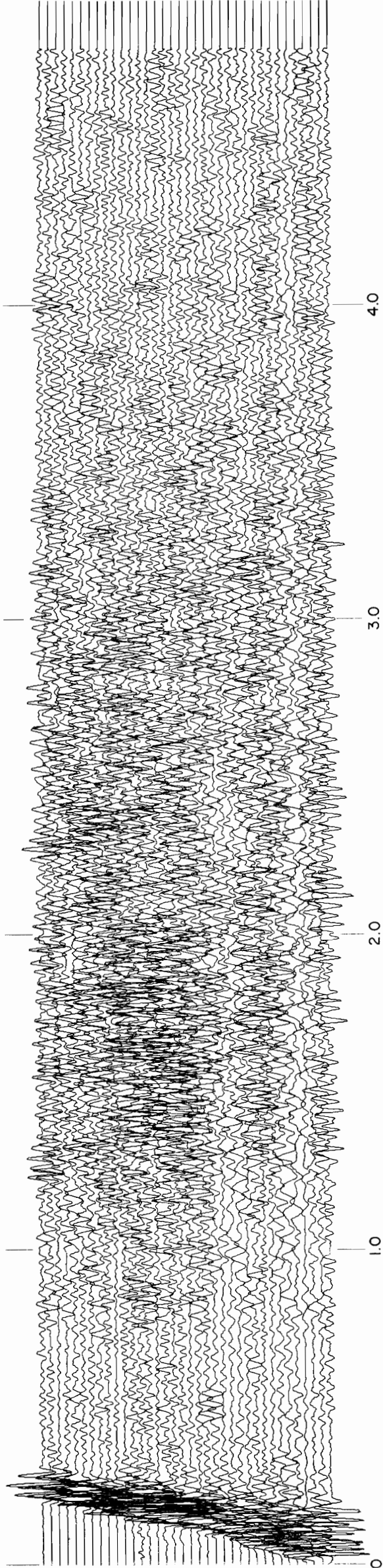
SECONDS

FIGURE V-5

BANE 2-3 (SHOTPOINT 5)
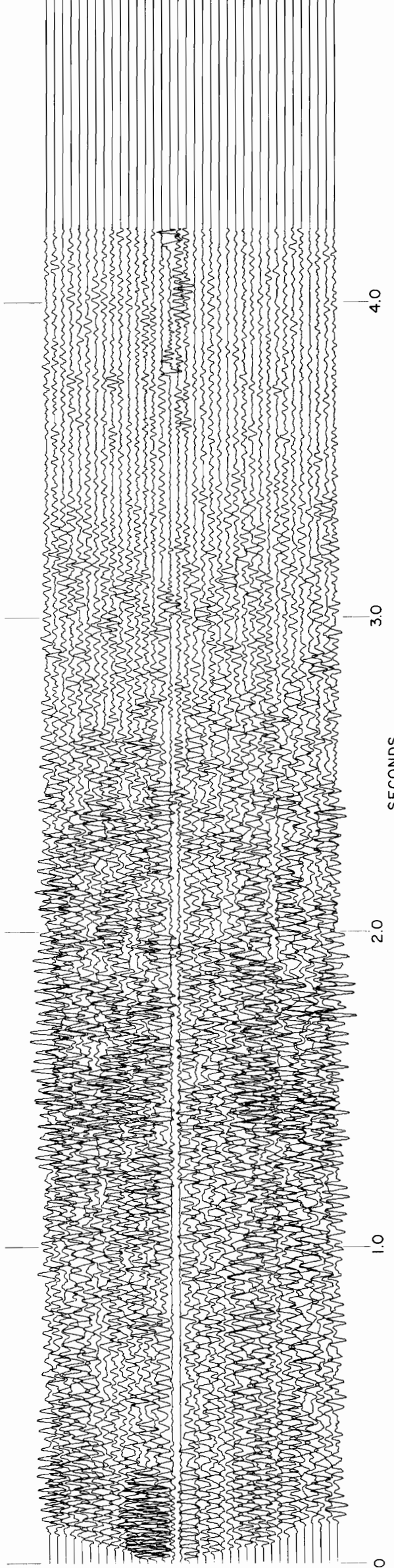
SECONDS

FIGURE V-6

BANE 2-4 (SHOTPOINT 6)

87
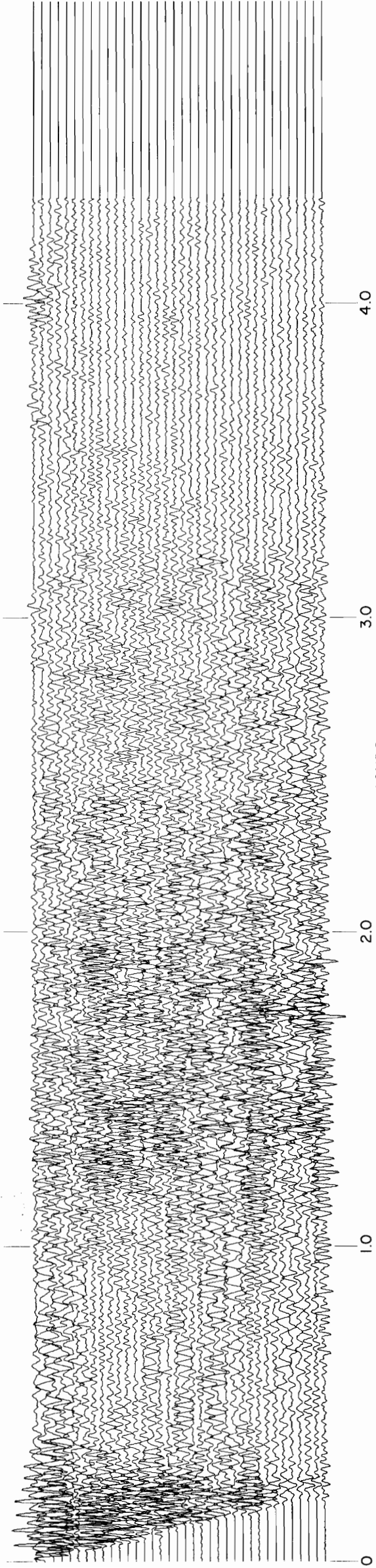
SECONDS
FIGURE V-7
BANE 3-1 (SHOTPOINT 7)
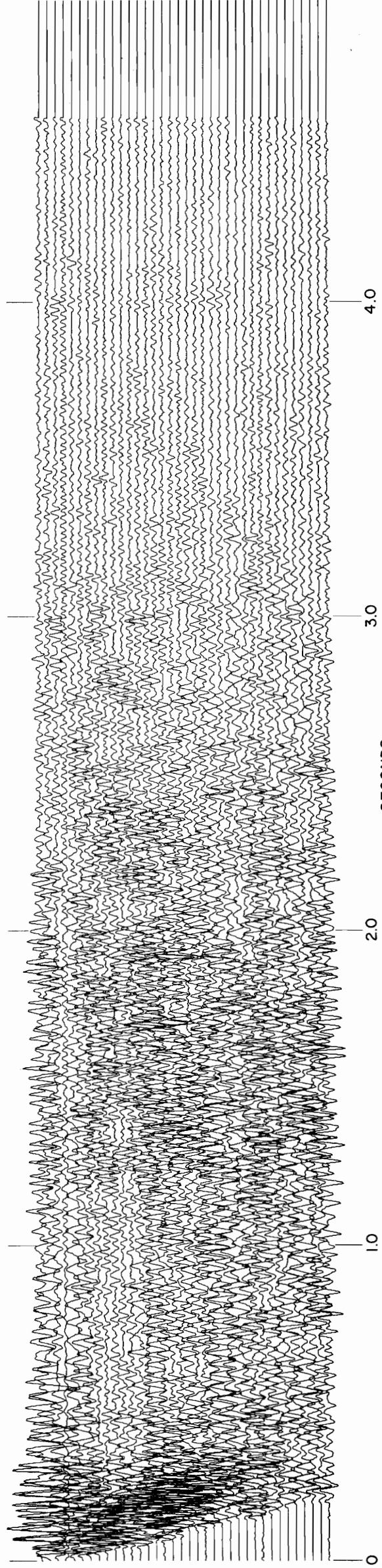
SECONDS
FIGURE V-8
BANE 3-2 (SHOTPOINT 8)

88
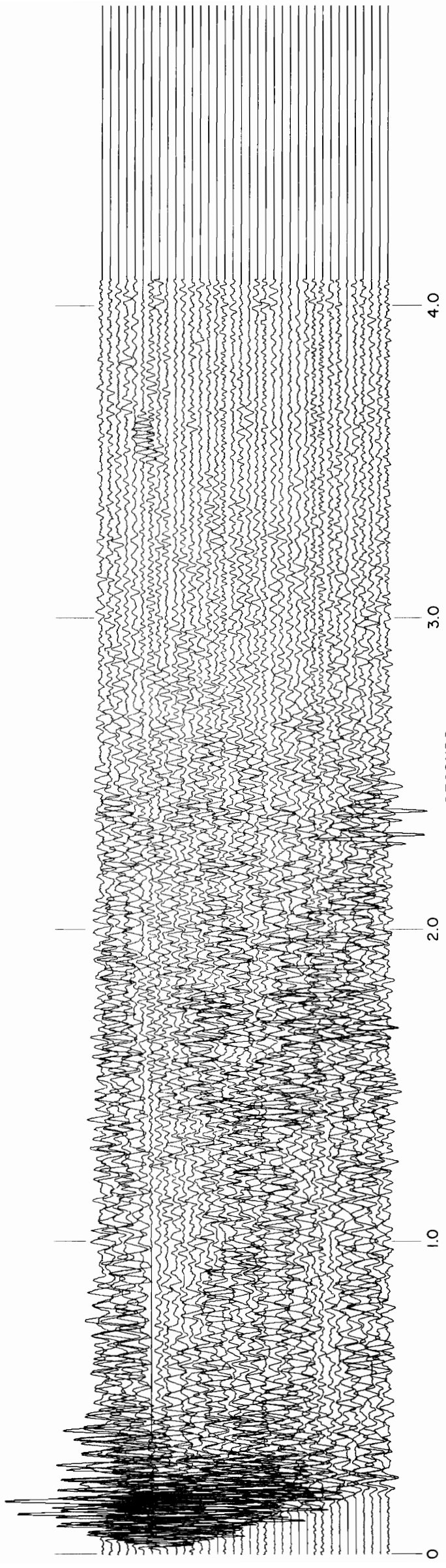
SECONDS
FIGURE V-9
BANE 3-3 (SHOTPOINT 9)

SECONDS
FIGURE V-IO
BANE 3-4 (SHOTPOINT IO)

89
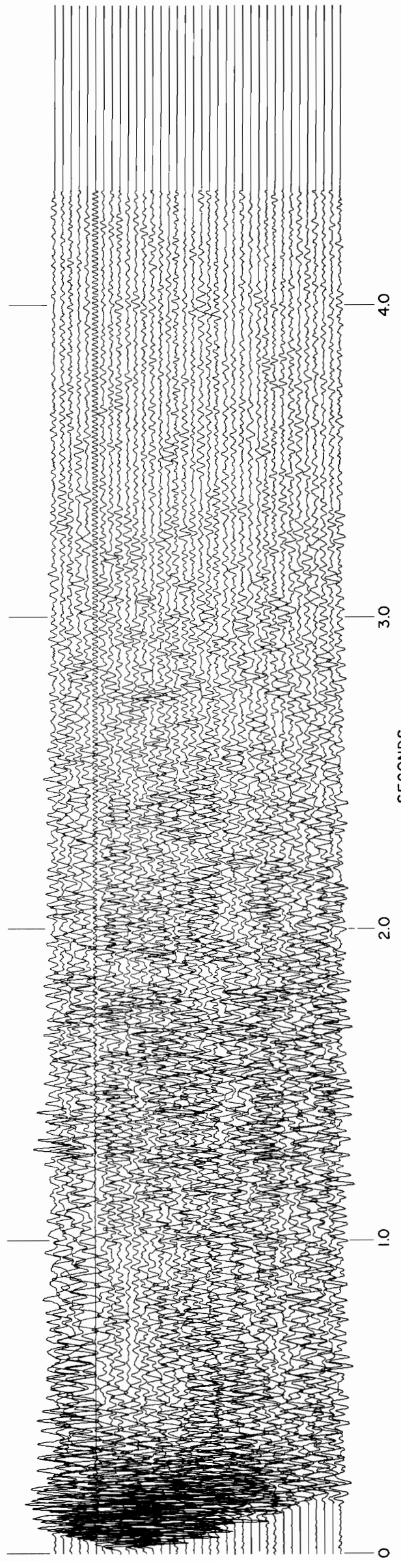
90
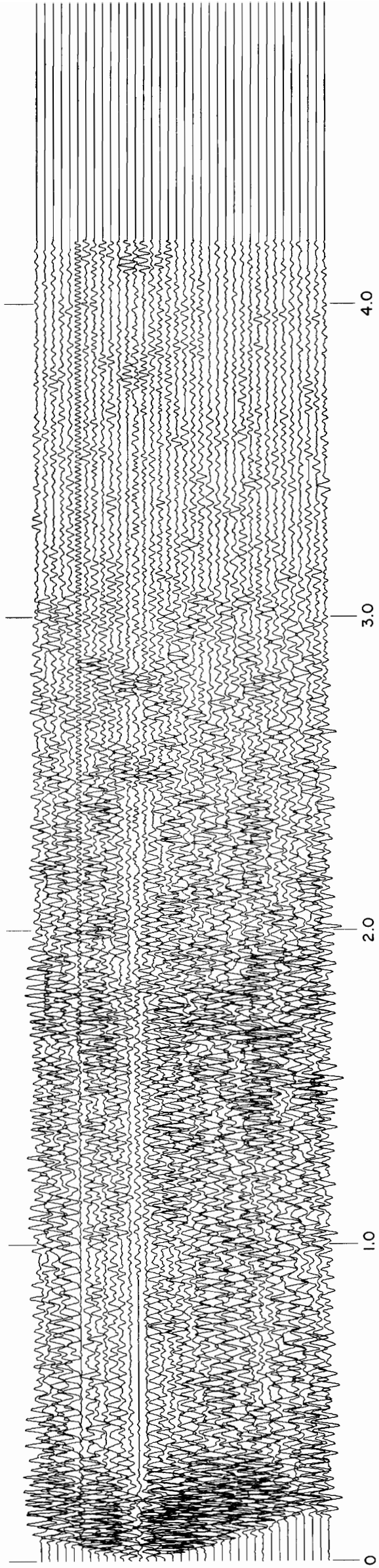
SECONDS

FIGURE V-11

BANE 3-5 (SHOTPOINT 11)

0   1.0   2.0   3.0   4.0

Appendix VI. Shotpoint-geophone distances

Tables VI-1 through VI-11 give the shotpoint-geophone distances for the eleven shotpoints of this study. These distances were scaled off graphically from an enlarged version of Figure 2. They were used in the RMS velocity analyses and in the generation of the synthetic seismograms in Figures 11 and IV-4.

TABLE VI-1

SHOTPOINT – GEOPHONE DISTANCES (meters)

<u>BANE 1-1</u>

GEOPHONE	DISTANCE	GEOPHONE	DISTANCE
1	612.0	19	90.5
2	582.2	20	62.2
3	552.6	21	31.4
4	523.3	22	3.9
5	494.1	23	27.1
6	467.3	24	58.2
7	436.8	25	82.3
8	407.5	26	111.9
9	377.6	27	141.1
10	345.9	28	167.3
11	319.7	29	199.3
12	285.1	30	228.9
13	257.6	31	260.0
14	226.5	32	285.9
15	201.2	33	317.3
16	177.7	34	345.6
17	147.5	35	374.9
18	119.8	36	403.3

TABLE VI-2

SHOTPOINT — GEOPHONE DISTANCES (meters)

BANE 1-2

GEOPHONE	DISTANCE	GEOPHONE	DISTANCE
1	989.1	19	485.9
2	959.8	20	457.8
3	932.4	21	427.3
4	904.3	22	398.7
5	875.7	23	370.0
6	850.7	24	340.5
7	822.0	25	316.7
8	793.7	26	287.1
9	765.4	27	257.3
10	737.9	28	230.7
11	709.9	29	201.2
12	681.2	30	174.0
13	650.1	31	146.0
14	620.9	32	115.5
15	595.9	33	85.0
16	573.6	34	56.4
17	543.5	35	27.1
18	515.7	36	9.4

TABLE VI-3

SHOTPOINT – GEOPHONE DISTANCES (meters)

BANE 2-1

GEOPHONE	DISTANCE		GEOPHONE	DISTANCE
1	710.5		19	189.6
2	680.9		20	161.2
3	651.4		21	129.8
4	621.8		22	100.9
5	592.8		23	71.6
6	566.0		24	40.5
7	535.8		25	17.1
8	506.3		26	14.0
9	477.0		27	43.9
10	448.1		28	70.4
11	418.8		29	101.5
12	388.9		30	131.1
13	356.9		31	161.5
14	327.1		32	188.7
15	299.6		33	219.8
16	275.8		34	248.4
17	244.8		35	278.6
18	218.5		36	307.5

TABLE VI-4

SHOTPOINT — GEOPHONE DISTANCES (meters)

BANE 2-2

GEOPHONE	DISTANCE	GEOPHONE	DISTANCE
1	786.1	19	271.0
2	756.8	20	242.9
3	727.9	21	211.8
4	698.9	22	183.2
5	670.0	23	153.9
6	644.0	24	123.7
7	614.2	25	99.7
8	584.9	26	70.1
9	556.3	27	39.9
10	527.6	28	13.7
11	499.0	29	21.0
12	469.4	30	49.9
13	437.7	31	80.5
14	407.8	32	105.2
15	381.6	33	135.6
16	358.7	34	164.9
17	328.0	35	194.5
18	300.8	36	222.8

TABLE VI-5

SHOTPOINT – GEOPHONE DISTANCES (meters)

BANE 2-3

GEOPHONE	DISTANCE	GEOPHONE	DISTANCE
1	923.5	19	412.4
2	894.6	20	384.7
3	865.3	21	353.9
4	836.7	22	325.2
5	808.6	23	296.0
6	783.0	24	265.5
7	753.8	25	241.7
8	724.8	26	211.8
9	696.5	27	182.0
10	668.4	28	155.4
11	639.5	29	124.4
12	610.5	30	96.0
13	578.8	31	67.7
14	549.2	32	37.8
15	523.3	33	7.0
16	494.4	34	22.9
17	470.0	35	53.0
18	442.6	36	82.6

TABLE VI-6

SHOTPOINT – GEOPHONE DISTANCES (meters)

BANE 2-4

GEOPHONE	DISTANCE		GEOPHONE	DISTANCE
1	465.7		19	70.4
2	434.9		20	97.8
3	405.1		21	128.3
4	375.2		22	157.0
5	345.6		23	186.2
6	317.6		24	216.7
7	286.2		25	240.8
8	256.0		26	270.7
9	226.2		27	300.2
10	196.6		28	327.1
11	166.7		29	358.7
12	136.9		30	388.3
13	105.5		31	418.8
14	75.6		32	445.3
15	46.0		33	476.1
16	18.3		34	504.4
17	12.8		35	533.7
18	40.5		36	562.1

TABLE VI-7

SHOTPOINT - GEOPHONE DISTANCES (meters)

BANE 3-1

GEOPHONE	DISTANCE	GEOPHONE	DISTANCE
1	37.5	19	559.9
2	68.6	20	587.3
3	98.4	21	618.1
4	128.0	22	646.2
5	157.6	23	674.5
6	186.2	24	704.4
7	217.6	25	727.6
8	247.2	26	756.5
9	277.4	27	783.3
10	306.6	28	808.3
11	336.2	29	840.3
12	366.4	30	869.9
13	396.8	31	900.1
14	426.7	32	922.3
15	456.3	33	951.6
16	484.9	34	977.2
17	515.1	35	1004.0
18	534.6	36	1028.7

TABLE VI-8

SHOTPOINT — GEOPHONE DISTANCES (meters)

BANE 3-2

GEOPHONE	DISTANCE	GEOPHONE	DISTANCE
1	91.1	19	435.3
2	60.1	20	463.0
3	29.9	21	494.1
4	3.4	22	522.1
5	29.6	23	551.1
6	58.2	24	581.6
7	89.3	25	605.0
8	119.2	26	634.3
9	149.7	27	661.7
10	178.9	28	687.3
11	208.5	29	719.9
12	238.7	30	749.5
13	269.7	31	779.7
14	300.2	32	803.1
15	329.2	33	832.4
16	357.8	34	859.5
17	388.3	35	887.0
18	408.7	36	912.6

TABLE VI-9

SHOTPOINT — GEOPHONE DISTANCES (meters)

BANE 3-3

GEOPHONE	DISTANCE		GEOPHONE	DISTANCE
1	180.7		19	348.1
2	150.0		20	375.8
3	119.8		21	406.9
4	89.9		22	435.6
5	60.7		23	464.8
6	31.7		24	495.3
7	3.4		25	519.1
8	29.9		26	548.3
9	60.1		27	576.4
10	89.9		28	602.6
11	119.2		29	634.9
12	149.7		30	664.5
13	181.4		31	695.2
14	211.5		32	719.3
15	240.2		33	748.9
16	268.5		34	776.3
17	299.3		35	804.4
18	321.0		36	831.2

TABLE VI-10

SHOTPOINT — GEOPHONE DISTANCES (meters)

BANE 3-4

GEOPHONE	DISTANCE		GEOPHONE	DISTANCE
1	271.0		19	258.2
2	239.9		20	286.2
3	210.0		21	317.6
4	180.1		22	346.6
5	150.3		23	375.8
6	121.6		24	406.6
7	90.8		25	430.1
8	60.7		26	459.9
9	30.5		27	488.3
10	2.7		28	514.2
11	28.9		29	546.5
12	59.1		30	576.4
13	90.8		31	606.9
14	121.0		32	632.2
15	149.7		33	662.3
16	177.7		34	689.8
17	208.5		35	718.1
18	230.4		36	744.6

TABLE VI-11

SHOTPOINT — GEOPHONE DISTANCES (meters)

BANE 3-5

GEOPHONE	DISTANCE	GEOPHONE	DISTANCE
1	359.7	19	168.9
2	329.2	20	197.2
3	299.0	21	228.6
4	269.1	22	257.3
5	239.6	23	286.5
6	211.2	24	317.6
7	180.1	25	341.4
8	150.6	26	371.2
9	120.1	27	399.9
10	90.5	28	426.1
11	61.0	29	458.4
12	31.1	30	488.0
13	4.3	31	518.5
14	31.4	32	544.1
15	59.7	33	574.2
16	88.4	34	602.6
17	118.6	35	631.2
18	140.5	36	658.7

Appendix VII. Ultrasonic velocity measurements

Traveltimes were measured through cylindrical rock samples approximately 5.4 cm in diameter and ranging in length from 2.69 to 6.94 cm. Measurements were made in a Series 10 – 40 Triaxial Cell (Rockcell) manufactured by Structural Behavior Engineering Laboratories, Inc. During measurement, each sample was under hydrostatic pressures equivalent to 200, 400, and 600 ATM.

Since the piezometric transducers used for the source and receiver were mounted behind steel rams, it was necessary to determine the traveltime through the rams. This was done by plotting the traveltimes through several steel cylinders of varying thicknesses and observing the intercept time corresponding to zero thickness. The calibration curves and intercept times for 200, 400, and 600 ATM are shown in Figures VII-1 through VII-3.

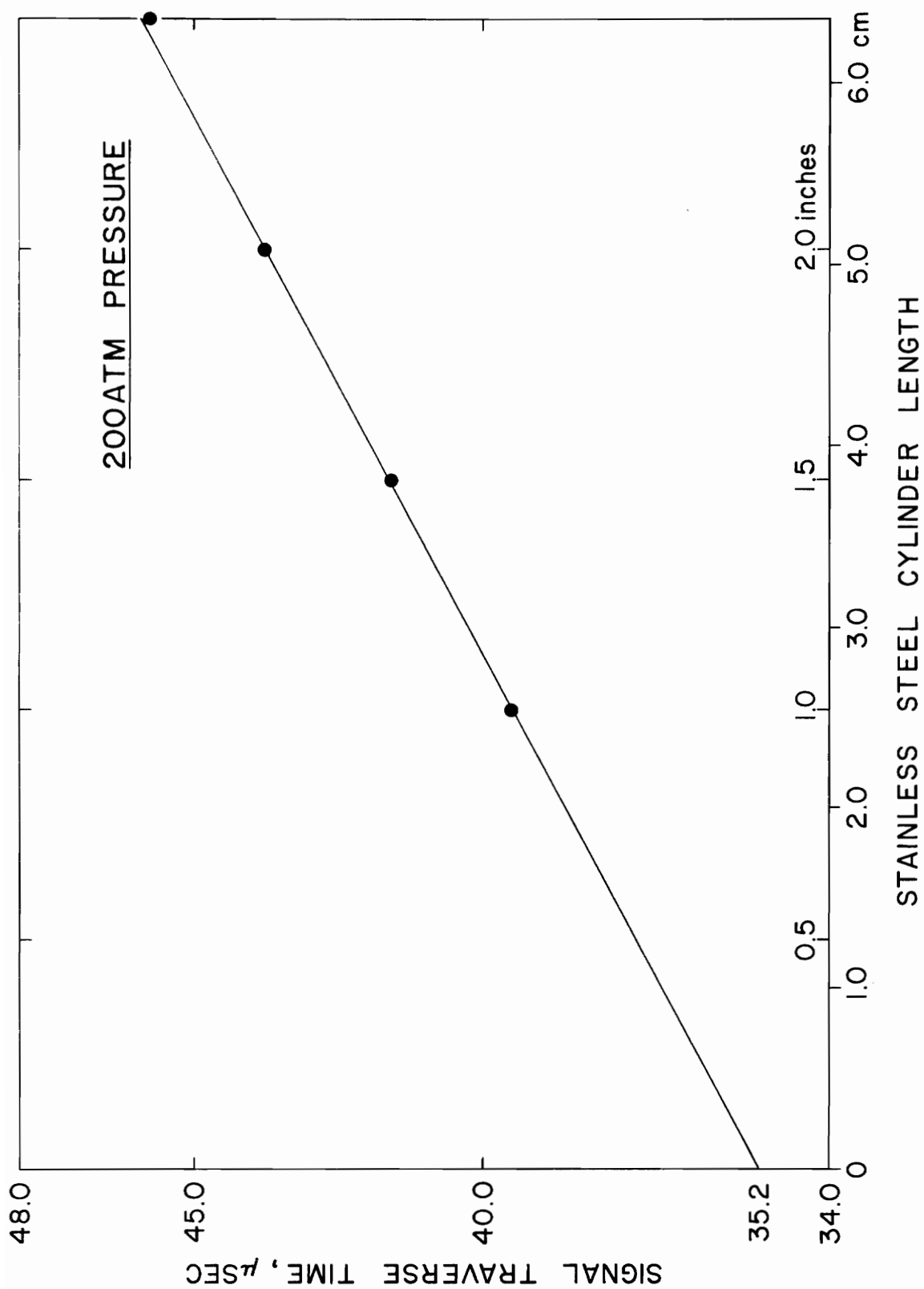The results of the velocity determinations are tabulated in the text as Table 2.

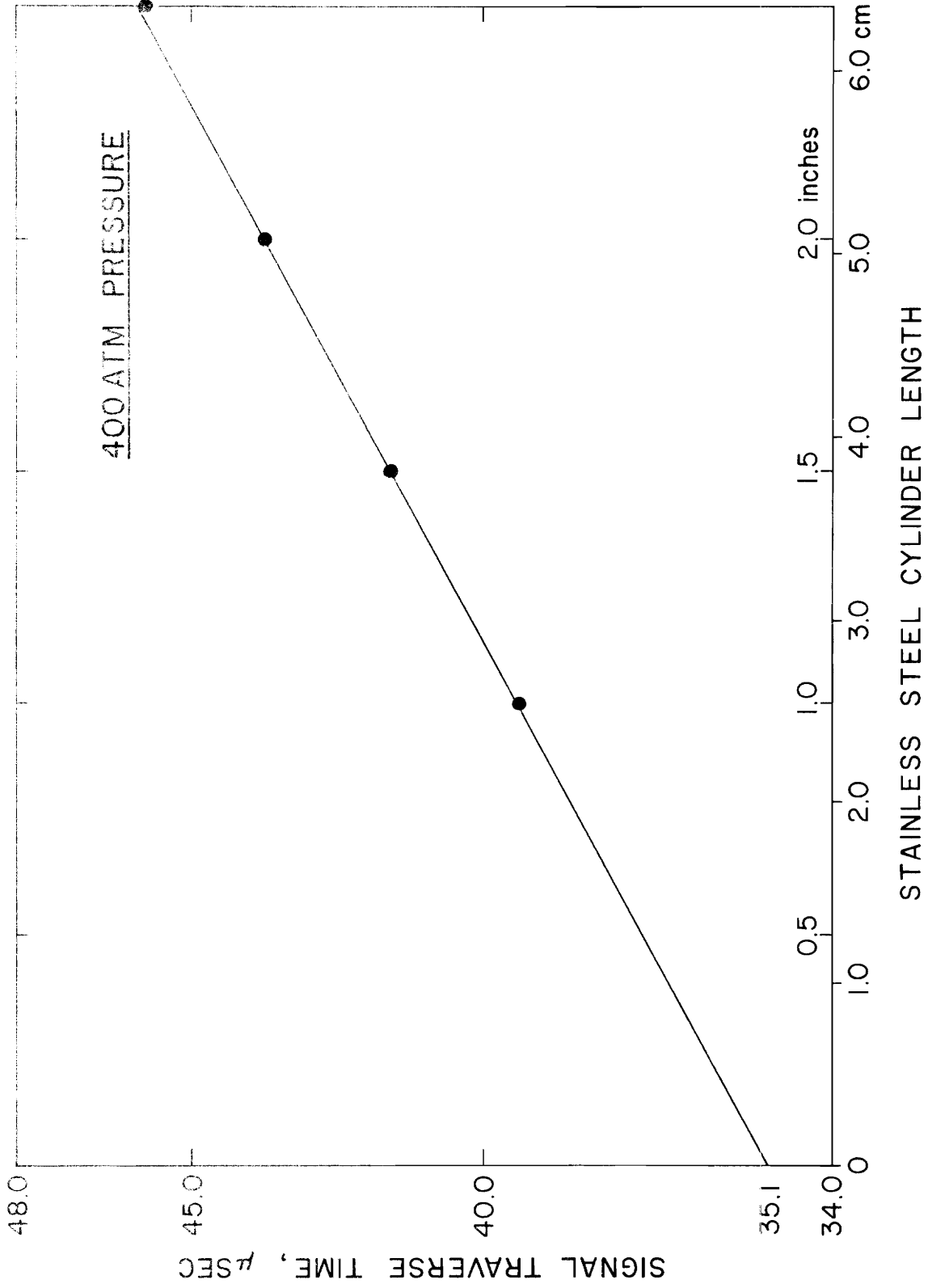Figure VII – I. Calibration curves for pressure cell.
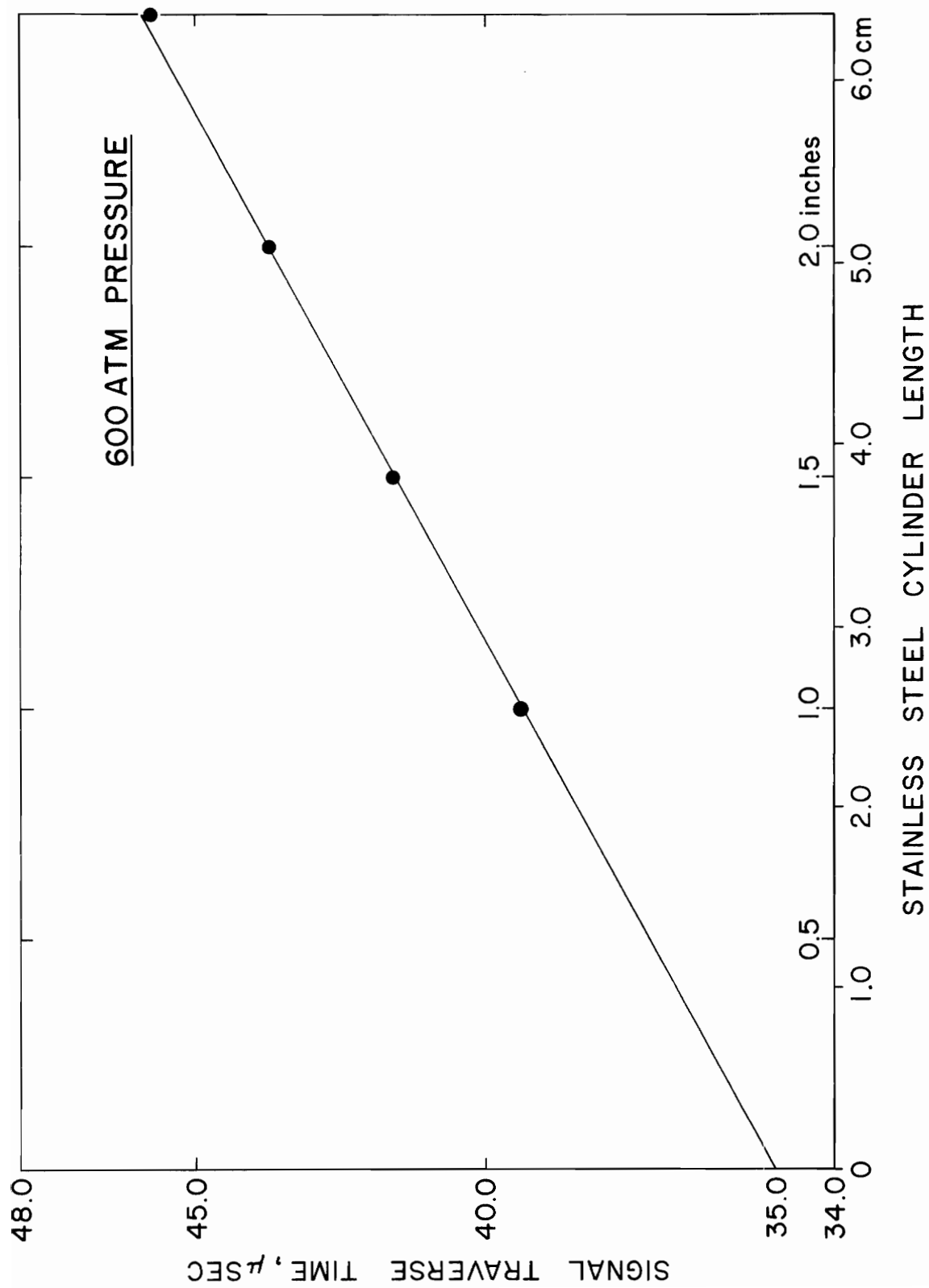
Figure VII - 2. Calibration curves for pressure cell.

Figure VII - 3. Calibration curves for pressure cell.

Appendix VIII. Study site

A portion of the Pearisburg, Virginia, $7\frac{1}{2}$-minute topographic map showing the location of the geophone spread used in this study is reproduced as Figure VIII-1.

Figure VIII - I. Location of geophone spread.

VITA

Robert William Edsall, Jr. was born September 24, 1945, in
Nyack, New York. He attended several elementary schools and Roy
W. Brown Junior High School in Bergenfield, New Jersey. He
graduated from Pulaski Academy and Central School in Pulaski, New
York, in June, 1963. He received his Bachelor of Science degree
in Geology from Rensselaer Polytechnic Institute in Troy, New
York, in June, 1967, at which time he was commissioned an Ensign
in the United States Navy. He terminated military service in
June, 1971, and enrolled in Graduate School the following
September at Virginia Polytechnic Institute and State University,
Blacksburg, Virginia, in the Department of Geological Sciences
as a Geophysics Major.

Robert W. Edsall, Jr.

A SEISMIC REFLECTION STUDY
OVER THE BANE ANTICLINE
IN GILES COUNTY, VIRGINIA

by

Robert W. Edsall, Jr.

(ABSTRACT)

A seismic reflection study over the Bane anticline in
southwest Virginia (37° 16' 50" N, 80° 41' 30" W) was made in an
attempt to gain information about the thickness of sedimentary
rocks in this part of the Appalachian Valley and Ridge province.
Eleven seismograms were obtained. In addition to frequency
filtering, velocity filtering, and deconvolution, new methods of
interpreting RMS velocity analyses were developed and applied.
Persistent events at about 1.0 and 2.8 seconds were found,
suggesting the presence of large reflection coefficients. On the
basis of ultrasonic velocity measurements made on rock samples
representative of the Cambrian sedimentary sequence and Precambrian
basement rocks believed to underlie the Bane anticline, it was
concluded that an unbroken Cambrian sequence overlying the basement
could not produce reflection coefficients of the magnitude
required, but that a thrust fault could. No definite conclusions
about the structure beneath the Bane anticline could be reached,

although the reflection at 2.8 seconds and the suggestion of a large reflection coefficient favor the interpretation of a thick, repeated sedimentary section.